THM modelling of Engineered Barriers for Spent Fuel Isolation

Erdem Toprak (UPC), Sebastia Olivella (UPC) and Xavier Pintado (B+TECH)

Abstract

This paper shows a comparison of 2D modelling corresponding to sensitivity analysis in the concept of KBS-3V. The backfill tunnel is decomposed into several components including Minelco granules and Rod pellets. Compared to previous studies (Posiva 2012-47), the pellet based components such as Rod pellets, Pillow pellets and Minelco granules are incorporated and simulated using BExM. In contrast, Friedland clay and MX-80 are simulated with BBM as usual. The gap between buffer and rock is considered to be filled with pillow pellets or remain empty so air and water will occupy the empty space.

1. Geometry, materials and initial conditions for reference model

In a reference model, drift backfill has three components: Friedland clay, Rod pellets and Minelco granules (foundation layer). The buffer has also three components: MX-80 bentonite, gap element at canister/buffer interphase and pillow pellets. The thickness of the canister/buffer gap element is 10 mm. A rock fracture is considered at the bottom of the buffer. The geometry, meshing and materials are shown in Figure 1. The geometry for backfill tunnel has been derived from previous studies. The foundation layer has 0.4 m of thickness and Rod pellets have a thickness of 0.3 m. The horizontal layer of highest permeability simulating a fracture has a thickness of 0.08 m.

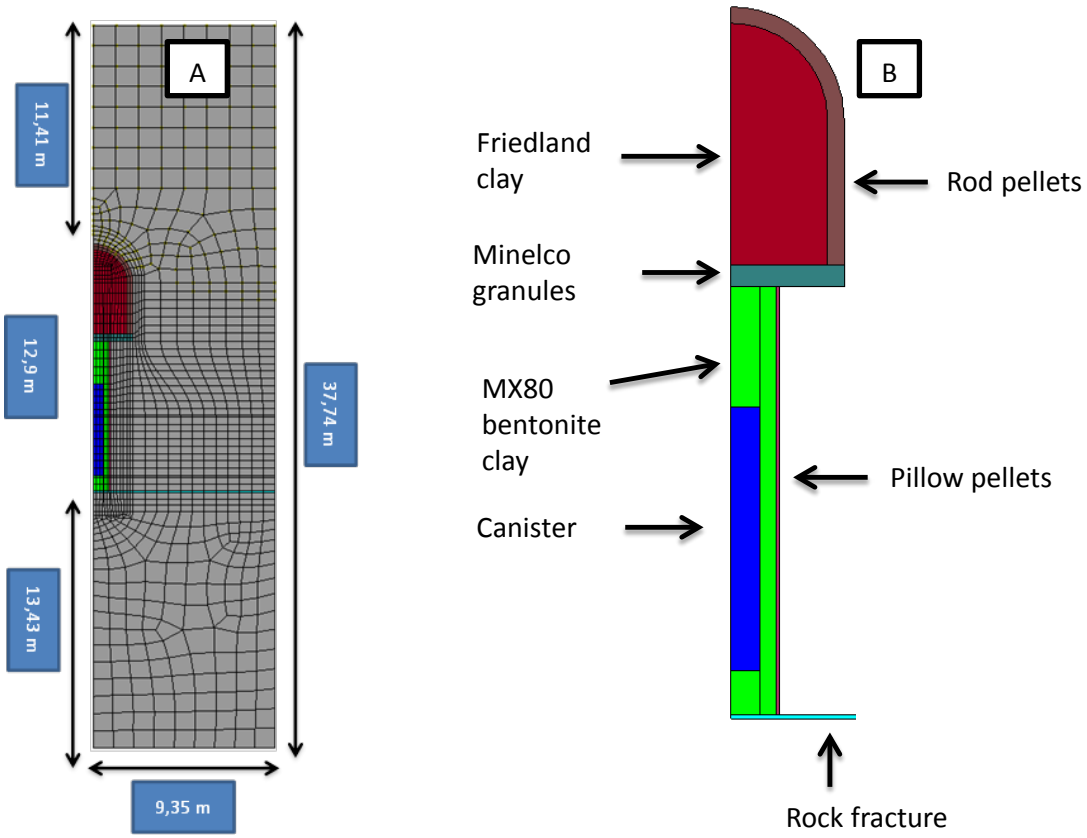

Figure 1. Geometry, mesh and materials in reference model

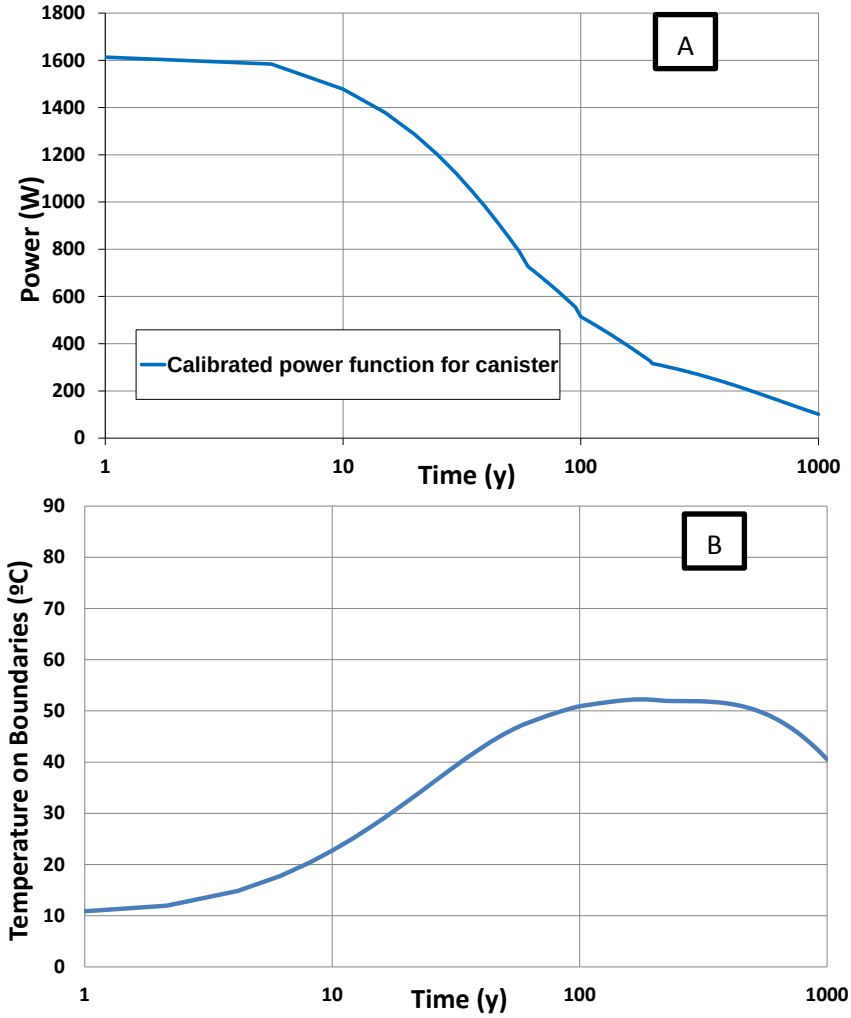

Figure 2. Power function for canister (A) and temperature on boundaries (B)

Table 1. Thermal parameters for materials

Parameters	Materials							
	Rock	Canister	Friedland-clay	Mx-80	Gap	Pellets		
						Rod	Pillow	Minelco
ρ_s (kg/m^3)	2749	7800	2780	2780	1.2	2780	2780	2780
ϕ_o	0.02	0.01	0.368	0.388	0.8	0.7	0.669	0.552
c_s (J/kgK)	784	450	800	800	1.0	800	800	800
λ_{dry} (W/mK)	2.61	390	0.3	0.3	0.045	0.3	0.3	0.3
λ_{dry} (W/mK)	2.61	390	1.3	1.3	0.6	1.3	1.3	1.3

An initial suction of 41 MPa is imposed for all components except the rock. In a first interval before barrier and backfill emplacement, excavation process is simulated. On the upper and lower boundaries, hydro-static water pressure is imposed. There is also water supply from the rock fracture. The system is confined. With regard to thermal conditions; a heat flow from canister is modelled as volumetric flow considering a time decay (Figure 2-A) and the upper and lower boundaries have prescribed temperature (Figure 2-B) obtained from uncoupled thermal modelling. Thermal parameters for materials are

summarized in Table 1. Hydraulic parameters for pellets, minelco granules, Mx-80 and Friedland clay have been calibrated through infiltration tests and are given in Table 2 and Table 3.

Mechanical parameters for rock and canister have been provided by Posiva oy and B+Tech. The mechanical parameters for gap element permit to model its closure in a simple way. Table 4 summarizes rock and gap mechanical parameters. The BBM parameters for MX-80 and Friedland clay and also BexM parameters for rod pellets, pillow pellets and minelco granules have been derived from oedometer and infiltration tests. These parameters are listed in Table 5.

Table 2. Hydraulic parameters of Rock, Friedland-clay, Mx80 and gap element

Parameters	Materials			
	Rock	Friedland-clay	Mx-80	Gap
P (MPa)	1.5	25	31.25	0.001
λ (-)	0.3	0.4	0.5	0.5
a (-)	-	-	-	10
k (m2)	$1.5x10^{-20}$	$1.6x10^{-20}$	$5.6x10^{-21}$	10^{-16}
m (-)	3	3	3	3
τ (-)	0.4	0.4	0.4	0.4

Table 3. Hydraulic parameters of Pillow pellets, rod pellets and minelco granules

Parameter	Pillow pellets	Rod pellets	Minelco granules	Unit
Po	5	5	5	MPa
λ	0.35	0.35	0.35	-
k0	$5x10^{-19}$	$1.4x10^{-18}$	$1.5x10^{-19}$	m2
ϕo	0.319	0.35	0.302	-
b	10	10	10	-
A (constant for krl)	1	1	1	-
m (power for krl)	3	3	3	-
τ (tortuosity)	0.4	0.4	0.4	-
Micro porosity	0.35	0.35	0.25	-

Table 4. Mechanical parameters for rock, canister and gap element

Parameter	Rock	Canister
E (MPa)	65000	21000
n	0.25	0.3
α (oC-1), linear	10^{-5}	10^{-5}

Parameters	Gap Element
Ec (MPa)	1000
n	0.3
α (oC-1), linear	-
Eo (MPa)	1
Strain limit	0.95

Table 5. Mechanical parameters for Mx-80, Friedland clay (BBM) and pillow, rod pellets and Minelco granules (BexM)

Parameters(BBM)	Symbols	Units	MX80	Friedland clay
Poisson ratio	ν	-	0.3	0.3
Minimum bulk module	Kmin	MPa	10	10
Reference mean stress	p_{ref}	MPa	0.01	0.01
Parameters for elastic volumetric compressibility against mean stress change	κ_{i0}	-	0.09	0.05
Parameters for elastic volumetric compressibility against suction change	κ_{s0}	-	0.09	0.05
Slope of void ratio-mean stress curve at zero suction	$\lambda(0)$	-	0.25	0.18
Parameters to define LC yield curve	r		0.8	0.8
	β	MPa^{-1}	0.02	0.02
Initial preconsolidation mean stress	P_o*	MPa	2	2
Critical state line	M	-	1.07	1.07

Parameter BexM	Pillow pellets	Rod pellets	Minelco Granules
κ^{Macro}	0.045	0.045	0.045
κ^{micro}	0.045	0.045	0.045
κ_s^{Macro}	0.01	0.01	0.01
ν^M	0.3	0.3	0.3
f_{sd0}	-0.1	-0.1	-0.1
f_{sd1}	1.1	1.1	1.1
n_{sd}	2	2	2
f_{si0}	-0.1	-0.1	-0.1
f_{sd1}	1.1	1.1	1.1
n_{si}	0.5	0.5	0.5
M	1	1	1
r	0.8	0.8	0.8
β	0.0001	0.0001	0.0001
p_c	0.1	0.1	0.1
P_{to}	0.01	0.01	0.01
$\lambda(0)$	0.19	0.3	0.3
P_0^*	2	4	4

2. Sensitivity analyses on filling material

The gap between rock and buffer can be filled with pillow pellets (pellet-gap) or air-water (empty-gap). A sensitivity analysis has been performed to investigate the choice of the filling material on the model results. Figure 3 shows thermal and mechanical response of the corresponding models. The canister-buffer gap is always empty (i.e. containing air-water).

The canister-buffer gap produces thermal isolation while remaining open (air has lower heat transport capacity than water or soil). For the rock-buffer gap the effect of filling or not with pellets is significant. Pellet-gap has higher thermal conductivity than empty-gap (containing air or water). Pellet-gap has lower

hydraulic conductivity than empty-gap. Pellet-gap delays the saturation and hence it delays the gap closure as compared to the empty-gap. This is explained by the slow saturation of the buffer as compared to the case of empty rock-buffer gap. The case with empty-gap leads to earlier closure of the gap, thus producing a decrease of temperature before 1 year. The peak temperature in the canister is lower for pellet-gap because its larger thermal conductivity. The peak caused by gap closure occurs earlier than the peak caused by the power decaying function, when the filling material is air-water (empty-gap).

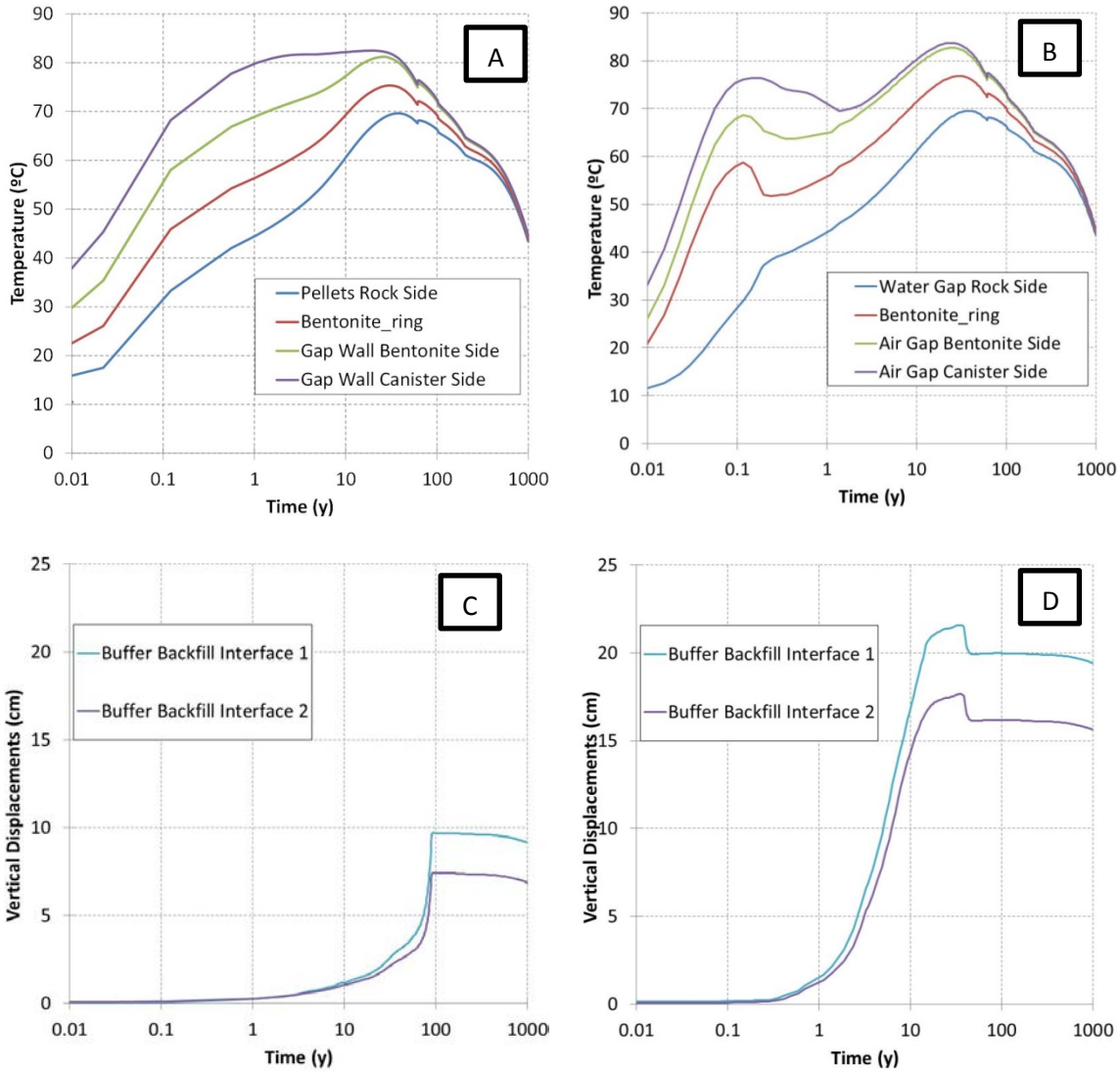

Figure 3. Evolution of temperature (A: pellet filling, B: water filling) and vertical displacements in both models (C: pellet filling, D: water filling)

Figure 3 shows also the vertical displacement evolution at the buffer backfill interface (design variable). When the gap filling material is air-water, buffer blocks swell considerably. The generated displacements due to swelling of buffer are two times higher than in the case of pellet filled gap.

Figure 4 shows evolution of total and micro porosity of rod and pillow pellets, and minelco granules. As the buffer hydrates progressively, macro pores close due to micro porosity increase. Figure 4A shows the case of gap filled with pillow pellets (pellet-gap). As a consequence of saturation, micro porosity of pellets increases which in turn leads to macro porosity reduction (small total volume variation). In other words, total porosity does not change considerably.

It can be seen that total porosity of rod pellets in both cases is practically constant. The reason is that, the saturation of rod pellets is slower and therefore, the micro and macro porosity change accordingly.

In Figure 4B, the results are shown for the empty-gap case modelling (i.e. pillow pellets do not exist). Swelling takes place earlier than in the pellet-gap. Rod pellets and Minelco granules undergo microporosity increase while total porosity remains nearly constant.

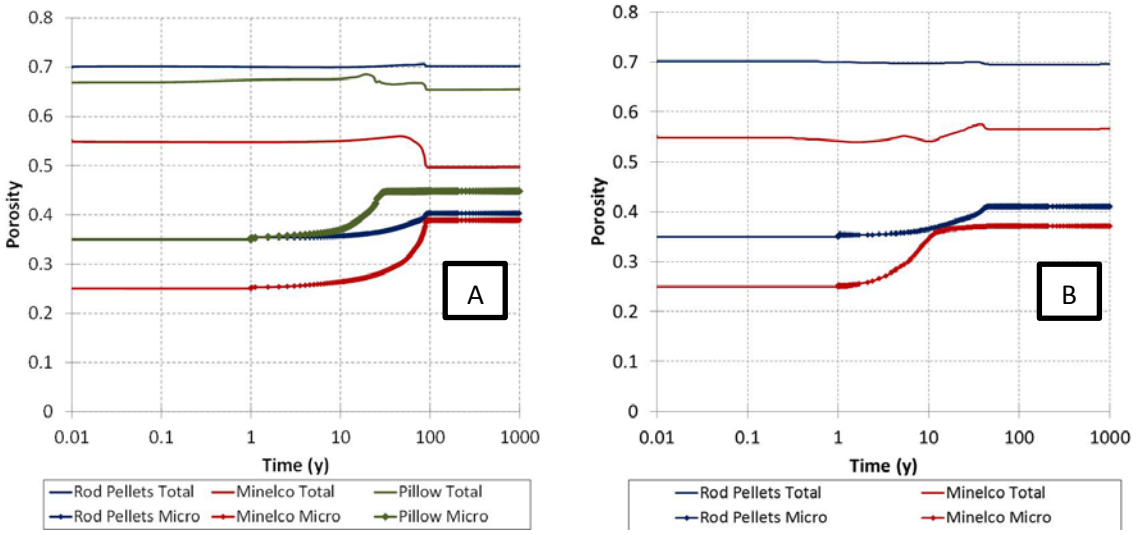

Figure 4. Evolution of total and micro porosity (A: pellet filling, B: water filling)

3. Conclusions and Future Work

An example of 2D sensitivity analysis has been described in this paper. BBM parameters for MX80 and Friedland Clay, BexM parameters for pillow pellets, rod pellets, and Minelco granules have been used (calibrated from oedometer and infiltration tests). When rock-buffer gap is empty (air-water), displacements increase significantly as compared with the case of rock-buffer gap filled with pellets. Calculated temperatures follow similar trend but some differences are attributed to the different thermal and hydraulic properties of the gap (pellet-gap vs empty gap).

Future work includes to investigate the effect of salinity of water, rock permeability, position of the fracture, thickness of the rock-buffer gap, thickness of the bottom layer (between buffer and backfill) and type of buffer material (can be either Mx80 or Febex bentonite).

4. References

Åkesson, M., Kristensson, O., Börgesson, L. (2010). SR-Site Data Report. THM modelling of buffer, backfill and other system components. Critical processes and scenarios. SKB TR-10-11. (www.skb.com/publication/2095121/TR-10-11.pdf) Stockholm. Sweden.

Alonso, E.E., Gens, A., Josa, A. (1990). A constitutive model for partially saturated soils. Géotechnique 40(3): 405-430

Marjavaara, P., Kivikoski, H. (2011). Filling the Gap between Buffer and Rock in the Deposition Hole. Posiva Working Report 2011-33. (www.posiva.fi/files/1923/WR_2011-33web.pdf) Eurajoki. Finland

Pintado, X., Mamunul, H. Md., Martikainen, J. (2013). Thermo-Hydro-Mechanical Tests of Buffer Material. Posiva Report 2012-49. ISBN 978-951-652-231-2, ISSN 1239-3096, Eurajoki. Finland

Toprak, E., Mokni, N., Olivella, S., Pintado, X. (2013). Thermo-Hydro-Mechanical Modelling of Buffer, Synthesis Report. Posiva Report 2012-47. ISBN 978-951-652-229-9, ISSN 1239-3096 Eurajoki. Finland

SENSITIVITY ANALYSIS OF COUPLED THERMO-HYDRO-MECHANICAL MODELS FOR EXPANSIVE CLAY SEALING SYSTEMS IN DEEP GEOLOGICAL DISPOSAL OF RADIOACTIVE WASTE

A. Rodriguez-Dono[*] and S. Olivella[*]

[*] Department of Civil and Environmental Engineering
Technical University of Catalonia (UPC)
Campus Nord UPC, 08034 Barcelona, Spain
e-mail: code.bright@upc.edu, web page: www.etcg.upc.edu/recerca/webs/code_bright/

Key words: Expansive clay, THM coupled analysis, radioactive waste disposal

Abstract. *This paper deals with the coupled thermo-hydro-mechanical (THM) behaviour of expansive clays in the deep geological disposal of radioactive waste. Some basic modelling work has been done in different codes, including Code_Bright, in order to make a verification of all the codes involved in this research and make the possible differences in the results appear explicitly. In this paper we show two different THM models and analyse the results obtained.*

1 INTRODUCTION

Deep geological storage or disposal remains the preferred option for waste management of heat-emitting, high-level radioactive nuclear waste (HLW) in several countries.

The required degree of waste isolation needed for HLW is provided by a combination of engineered and natural barriers placed between the potentially harmful radionuclides and the biosphere. The natural barrier is fundamentally the host rock, and the artificial barriers are the solid matrix of the waste itself, the metallic canister enclosing the waste, and the backfill −the sealing material placed around the canisters. This backfill, also called an 'engineered barrier', is often constructed using compacted expansive clay. Bentonite has generally been chosen because of its high swelling capacity, low permeability and favourable retardation properties[i].

The bentonite barrier fulfils several important functions. In the first instance, a very low hydraulic conductivity restricts water penetration and retards significantly solute transport due to its low diffusion coefficient and to additional sorption effects. It should also provide a favourable chemical environment and be able to self-heal if subjected to physical perturbation such as cracking and fissuring events[ii]. The engineered clay barrier and adjacent host rock (usually called the 'near field') will be subjected to the heating effect of the nuclear waste, and also to various associated hydraulic and mechanical phenomena that interact in a complex way.

In addition, compacted bentonite is initially unsaturated, and will therefore be subjected to hydration from the surrounding rock, triggering further coupled thermo-hydro-mechanical (THM) phenomena. In order to achieve a safe and robust repository design, it is necessary to have a good understanding of the processes that occur in the near field, and of their evolution over time[i].

Given the importance of the problem, it has proved useful to perform large-scale and

medium-scale heating tests simulating repository conditions in underground laboratories around the world[iii,iv,v,vi]. Because of the low permeability of the materials involved, such experiments usually require long testing times, measured in years, in order to obtain meaningful results. The complexity of the phenomena involved, and of their interactions, implies that process understanding and interpretation of results are limited unless supported by suitable numerical models able to reproduce the main features of the test. Owing to the coupled nature of the THM interactions, coupled THM formulations are inevitably required.

In this paper, and in the context of the Engineered Barrier System (EBS) Task Force research, a number of basic modelling work has been done in different codes, including Code_Bright[vii], OGS and Tough-FLAC, in order to make a verification of all the codes involved in this research and make the possible differences in the results appear explicitly.

Code_Bright[vii] is a Finite Element Method (FEM) program that enables coupled thermo-hydro-mechanical analysis in geological media. This is a code version that incorporates customized pre- and post- process interfaces so that simulation models that use Code_Bright −available from: bit.ly/code_bright− can be developed more easily. It allows easy modification of parameters, boundary conditions, excavation protocols, meshing and organization of calculation intervals. The reason is that it has been developed using the GiD interface (http://www.gidhome.com) that permits pre- and post- process of data in a user-friendly way.

In this paper we show two different THM models: one very basic model considering elastic material behaviour and a more complex one taking also into account a linear swelling behaviour of the bentonite.

2 MODEL DESCRIPTION

The code comparison is thus divided in the two following stages with increasing complexity of the THM coupled simulation:

- Elastic material behaviour.
- Elastic material behaviour + linear swelling of the bentonite.

The base case model represents a single deposition hole in a 2D axisymmetric model (Figure 1). The different bentonite elements are simplified to a homogeneous buffer material. Access tunnel and backfill material are neglected. To reduce the mesh size, the canister is not discretized; instead the heat source term is applied to the canister-buffer interface.

The calculation is divided into two phases –a purely hydraulic calculation of the open deposition hole and the TH(M) calculation of the time after deposition of the waste canister (Table 1). For the first phase, steady state is assumed to be reached. The boundary and initial conditions applied to the model are summarized in Figure 2.

The heating of the canister is simulated by applying a power as a boundary condition in the canister boundary, the evolution of which is shown in Figure 3 (the initial power is 1700 W).

Two different materials are considered in this model: The bentonite and the host rock, which properties will not be shown in this paper for the sake of briefness, but are available for anybody interested just asking for them by e-mail to the authors. The mechanical models used are a linear elastic one for the rock in all models and also for the bentonite in the most basic case. In the case of swelling of the bentonite being taken into account, a termo-elasto-plastic model (TEP) is considered. More information about the models in the Code_Bright Users's Guide, downloadable from the Code_Bright website.

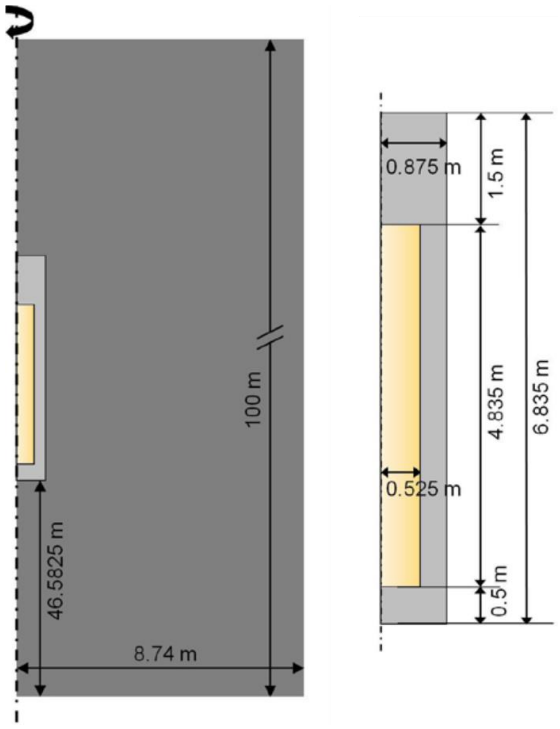

Figure 1: Model dimensions

Phase	Description	Duration	Processes
1	Open deposition hole	Steady state	H
2	Installed canister and buffer / canister heating	1000 years	THM

Table 1: Base case calculation sequence

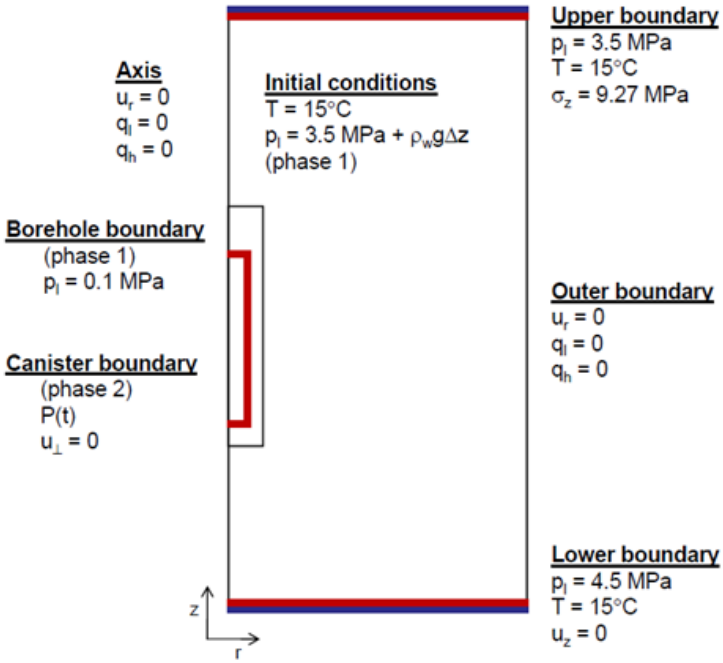

Figure 2: Boundary and initial conditions

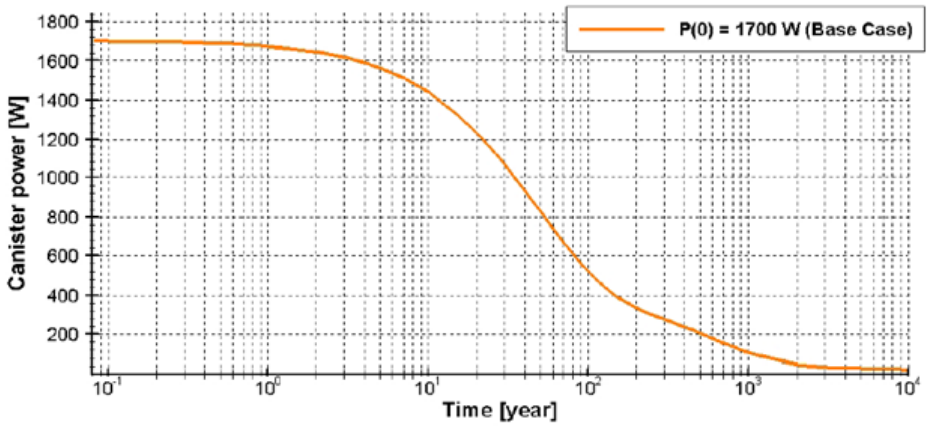

Figure 3: Canister power evolution

Two different materials are considered in this model: The bentonite and the host rock, which properties will not be shown in this paper for the sake of briefness, but are available for anybody interested just asking for them by e-mail to the authors. The mechanical models used are a linear elastic one for the rock in all models and also for the bentonite in the most basic case. In the case of swelling of the bentonite being taken into account, a thermo-elasto-plastic model (TEP) is considered. More information about the models in the Code_Bright Users's Guide, downloadable from the Code_Bright website.

3 RESULTS

3.1 THM analysis with elastic material behaviour

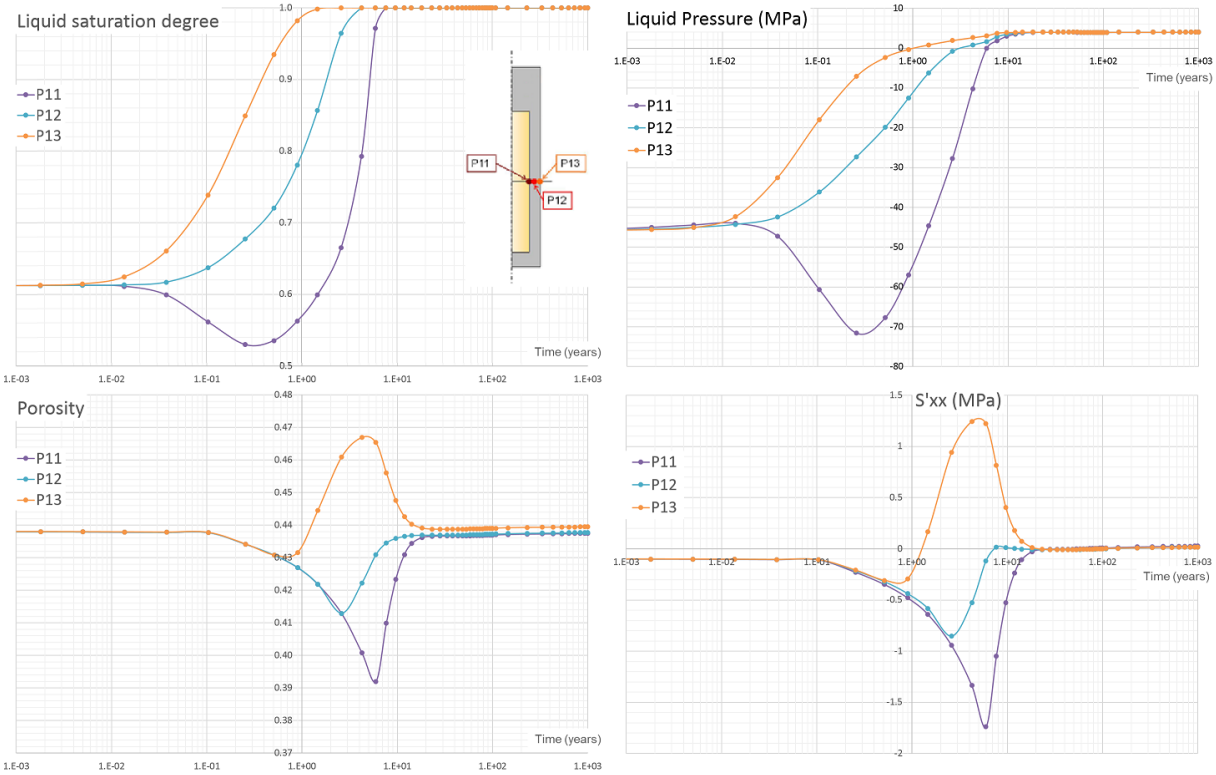

3.2 THM analysis with elastic material behaviour + linear swelling of bentonite

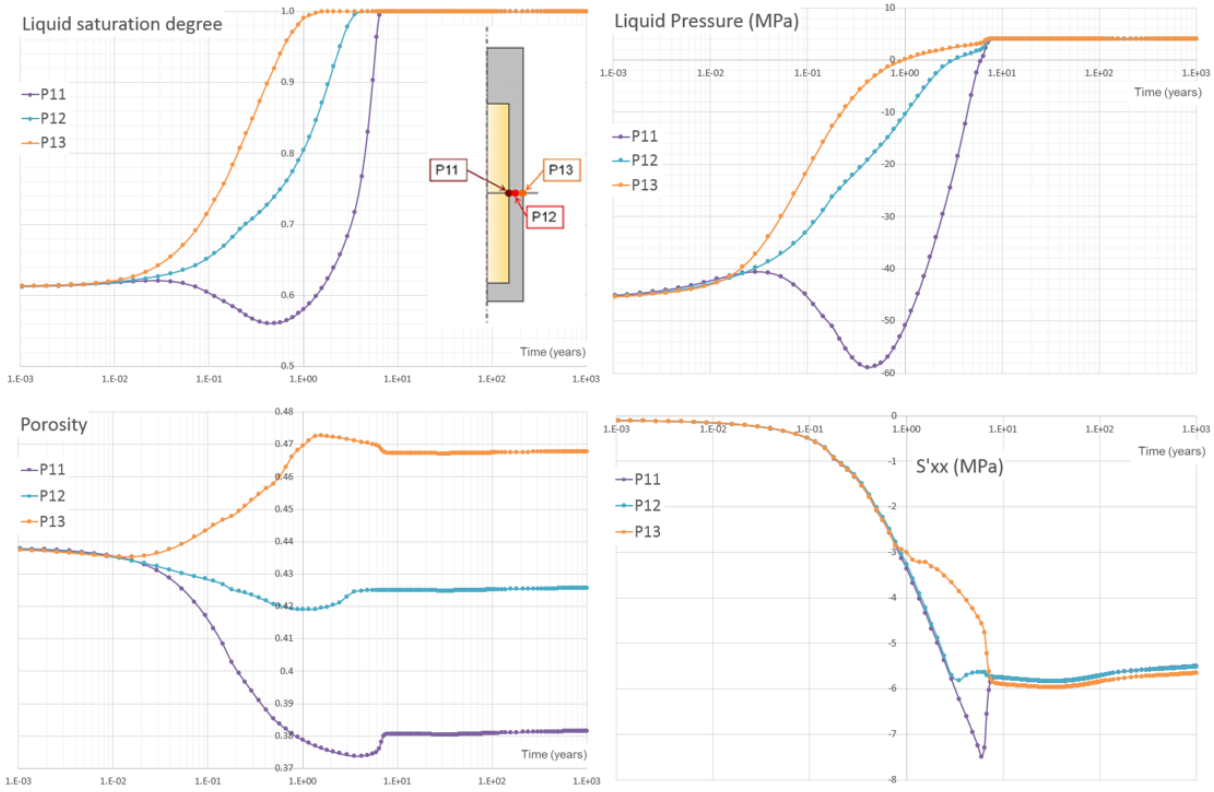

4 CONCLUSIONS

Two THM different models have been used to show the differences in the results when taken into account the swelling of the bentonite compared to a basic model that doesn't take into account this behaviour. We have observed that the temperatures don't get significantly affected by this swelling behaviour and the liquid saturation degree and the liquid pressure are moderately affected specially in the zone close to the heater. However, the porosity values and the stresses are very affected by the swelling behaviour. In fact, and as it would be expected, the stress values are much higher when considering swelling. And these differences in stresses also affect significantly the porosity.

The purpose of this work is the validation of the code and the understanding of the behaviour of the bentonite. Further research is needed, but we hope this simple model can give some insight to this complex problem.

REFERENCES

[i] Gens A, Sanchez M, Guimaraes LDN, Alonso E, Lloret A, Olivella S et al. A full-scale in situ heating test for high-level nuclear waste disposal: observations, analysis and interpretation. Geotech. 2009;59(4):377-99. doi: 10.1680/geot.2009.59.4.377

[ii] Gens A. The role of geotechnical engineering in nuclear energy utilisation: special lecture. In: Proc 13th Eur Conf Soil Mech Geotech Eng, Prague; 2003;3:25-67.

[iii] Dixon D, Chandler N, Graham J, Gray MN. Two large-scale sealing tests conducted at Atomic Energy of Canada's underground research laboratory: the buffer-container experiment and the isothermal test. Can Geotech J. 2002;39(3):503-18.

[iv] Pusch R, Borgesson L, Ramqvist G. Final report of the mass buffer test -volume II: Test results, Stripa Project 85/12. Stockholm: SKB; 1985.

[v] Selvadurai APS. Hydro-thermo-mechanics of engineered clay barriers and geological barriers. Eng Geol. 1997;47(4):311-2. doi: 10.1016/S0013-7952(97)00036-7

[vi] Volckaert G, Bernier F, Alonso E, Gens A, Samper J, Villar MV, Martin PL, Cuevas J, Campos R, Thomas HR, Imbert C, Zingarelli V. Thermal-hydraulic-mechanical and geochemical behaviour of the clay barrier in radioactive waste repositories (model development and validation), Nuclear Science and Technology, EUR 16744. Luxembourg: Commission of the European Communities; 1996.

[vii] Olivella S, Gens A, Carrera J, Alonso E. Numerical formulation for a simulator 'CODE_BRIGHT' for the coupled analysis of saline media. Engng Comput. 1996;13(7):87-112.

MODELLING OF THE HYDRO-MECHANICIAL BEHAVIOUR OF CLAY ROCK

Chun-Liang Zhang[a] and Alfonso Rodriguez-Dono[b]

[a] Gesellschaft für Anlagen- und Reaktorsicherheit (GRS)
Theodor-Heuss-Strasse 4, 38122 Braunschweig, Germany
e-mail: chun-liang.zhang@grs.de, web page: http://www.grs.de/

[b] Department of Civil and Environmental Engineering
Technical University of Catalonia (UPC), Campus Nord UPC, 08034 Barcelona, Spain
e-mail: alfonso.rodriguez@upc.edu, web page: http://www.upc.edu/

Key words: claystone, deformation, damage, permeability

1 INTRODUCTION

With regard to the German approach of the safe containment of radioactive waste in an isolating rock zone (IRZ), it is of paramount importance to reliably predict the long-term processes in the host rock, particularly the reversibility of the excavation damaged zone (EDZ) around the repository openings. In order to improve the constitutive models available from the THM code CODE_BRIGHT with respect to the long-term deformation, damage and permeability change in clay rock, a research programme (THM-TON) has being conducted by GRS, which is funded by the German Federal Ministry of Economics and Technology (BMWi). The modelling work has being supported by the code developer, UPC/CIMNE, within the frame of the consortium agreement. During the last years, GRS has established new constitutive equations for the claystone creep (Zhang, 2015) and the damage-induced permeability (Zhang, 2016). In parallel, UPC has enhanced its elastoplastic model with new formulations for strain hardening-softening, creep, and others (Ruiz et al., 2015). Some new models have been implemented in CODE_BRIGHT. The verification of the new models has been performed by numerical simulation of laboratory experiments and comparison with the test data.

2 CONSTITUTIVE MODELS

2.1 Visco-elastoplastic model

The new visco-elastoplastic model developed by UPC (Ruiz et al., 2015) accepts the Mohr-Coulomb criterion for yield surface in the stress space that separates the elastic and plastic parts of the mechanical response:

$$F = \left(\cos\theta + \frac{1}{\sqrt{3}} \sin\theta \cdot \sin\varphi \right) J - \sin\varphi \cdot (c\cot\varphi + p_t) \geq 0 \tag{1}$$

where θ is Lode's angle, φ is the friction angle, c is the cohesion depending on suction s by $c = c_o + s \cdot \tan\varphi$, and $p_t = c \cdot \cot\varphi$ represents the isostatic tensile strength.

For simplicity, the claystone is here assumed to be isotropic. The linear elastic behaviour is expressed as

$$d\sigma_{ij} = D^{e}_{ijkl}\left(d\varepsilon_{kl} - \delta_{kl}\frac{ds}{K_s} - d\varepsilon^{vp}_{kl} \right) \tag{2}$$

where σ_{ij} = effective stresses; ε_{kl} = total strains; ε^{vp}_{kl} = viscoplastic strains; D^{e}_{ijkl} = elastic stiffness matrix; K_s = bulk modulus against suction change ($s = p_g - p_l$) by a linear relationship of $d\varepsilon^{s}_{v} = ds / K_s$; and δ_{kl} = Kronecker delta.

An isotropic hardening-softening law is considered, governed by the evolution of the strength parameters (φ , c). The equivalent plastic deformation is the selected state variable to control this evolution, which is defined as:

$$\varepsilon^{p}_{eq} = \left(\frac{2}{3}\boldsymbol{\varepsilon}^{p} : \boldsymbol{\varepsilon}^{p} \right)^{1/2} \tag{3}$$

where $\boldsymbol{\varepsilon}^{p}$ is the plastic deformation tensor.

The way in which the angle of friction varies depends on the equivalent plastic deformation, as outlined in figure 1. The laws of evolution in each one of the listed areas are also shown. Cohesion evolves as a function of the mobilized friction angle and at any point is given by the following expression: $c_{mov} = c_{peak} \cdot \cot\varphi_{ini} \cdot \tan\varphi_{mov}$.

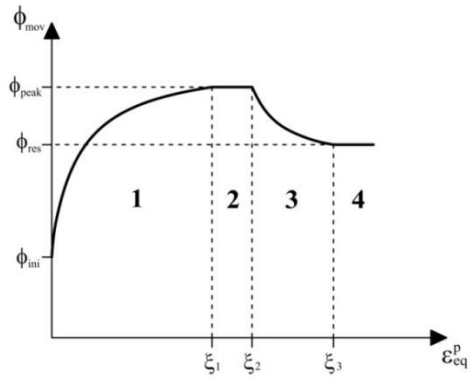

Zone 1 $\varphi_{mov} = \varphi_{ini} + \dfrac{\varepsilon^{p}_{eq}}{a_{hard} + \dfrac{\varepsilon^{p}_{eq}}{\Delta\varphi_{hard}}}$, $\Delta\varphi_{hard} = \dfrac{\xi_1}{\dfrac{\xi_1}{\varphi_{peak} - \varphi_{ini}} - a_{hard}}$

Zone 2 $\varphi_{mov} = \varphi_{peak}$

Zone 3 $\varphi_{mov} = \varphi_{peak} - \dfrac{\varepsilon^{p}_{eq} - \xi_2}{a_{soft} + \dfrac{\varepsilon^{p}_{eq} - \xi_2}{\Delta\varphi_{soft}}}$, $\Delta\varphi_{soft} = \dfrac{\xi_3 - \xi_2}{\dfrac{\xi_3 - \xi_2}{\varphi_{peak} - \varphi_{res}} - a_{soft}}$

Zone 4 $\varphi_{mov} = \varphi_{res}$

φ_{mov} = mobilized friction angle, φ_{ini} = initial friction angle at yield surface, φ_{peak} = peak friction angle at peak failure strength, φ_{res} = residual friction angle at residual strength, ξ_1 = equivalent plastic strain at which the maximum strength is reached, ξ_2 = equivalent plastic strain at which softening begins, ξ_3 = equivalent plastic strain at which the residual strength is reached, α_{hard} = constant that controls the curvature of the function in the hardening branch, α_{soft} = constant that controls the curvature of the function in the softening branch.

Figure 1 Evolution of the friction angle as a function of equivalent plastic deformation

For description of the creep, a modified Lemaitre law is adopted taking into account strain-hardening effect. The strain rate is expressed as function of deviatoric stress and equivalent plastic strain

$$\dot{\varepsilon}^{vp} = \gamma\left(q - \sigma_s\right)^{n}\left(1 - \varepsilon^{vp}_{eq}\right)^{m} \tag{4}$$

where γ is a parameter of viscosity, σ_s is a threshold of the deviatoric stress from which the viscoplastic deformation is activated, n and m are material constants and ε_{eq}^{vp} is the state variable of the viscoplastic response, defined as $\varepsilon_{eq}^{vp} = \int_o^t \left(\frac{2}{3} \dot{\boldsymbol{\varepsilon}}^{vp} : \dot{\boldsymbol{\varepsilon}}^{vp} \right)^{1/2} dt$.

2.2 Permeability model

Based on the laboratory observations, a new permeability model was developed for clay rock by Zhang (2016), which describes the permeability variation with dilatancy before and after failure.

$$\mathrm{k} = \begin{cases} k_c & (\sigma_1 - \sigma_3) < \sigma_B \\ k_o \cdot exp(-r\sigma_3) \cdot \left(1 - \exp\left(-\frac{\Delta\varepsilon_D}{\varepsilon_B}\right)\right) & \sigma_B \geq (\sigma_1 - \sigma_3) \geq \sigma_R \\ \mathrm{D} \cdot (\Delta\varepsilon_R)^3 & (\sigma_1 - \sigma_3) < \sigma_R \end{cases}$$

This model is schematically highlighted in figure 2 in terms of differential stress ($\Delta\sigma = \sigma_1 - \sigma_3$), volumetric strain ($\varepsilon_v$), and permeability (k) vs. axial strain (ε_1) for the pre- and post-failure stages.

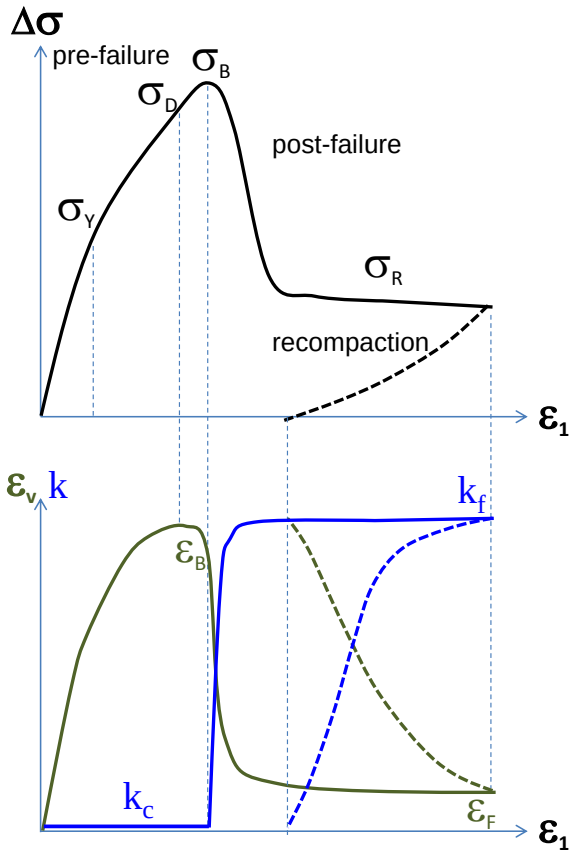

Figure 2 Stress-strain-permeability behaviour of claystone during damage and recompaction (σ_Y = yield stress, σ_D = dilatancy threshold, σ_B/ε_B = peak failure stress/volumetric strain, σ_R = residual strength, k_c = initial permeability, k_f = final fracture permeability at ultimate fracturing with the volumetric strain ε_F)

During the pre-failure phase, $(\sigma_1 - \sigma_3) < \sigma_B$, the very low permeability of the natural intact claystone does not increase but decreases slightly with volume compaction. For the purpose of simplification, the permeability value can be assumed constant (a). As measured, k_c–values of the COX and OPA claystones are in a range of $10^{-20} – 10^{-21}$ m^2. When the stress reaches the peak value $(\sigma_1 - \sigma_3) = \sigma_B$, the permeability begins to increase. Beyond that, $\sigma_B \geq (\sigma_1 - \sigma_3) \geq \sigma_R$, the fracturing-induced permeability increases rapidly with volumetric dilatancy. The permeability percolation is contributed by the connectivity and the conductivity of microcracks. It can be expressed with the percolation probability of cracks belonging to the conducting part of a network and the ultimate permeability after fully fracturing (b). The percolation probability is expressed as an exponential function of crack dilatancy: $p = (1 - \exp(-\Delta\varepsilon_D/\varepsilon_B))$, where $\Delta\varepsilon_D = |\varepsilon_v - \varepsilon_B|$ is the dilatancy with reference to the volumetric strain ε_B at the percolation threshold equal to the peak stress σ_B. The ultimate fracture permeability increases exponentially with decreasing the minor principle stress: $k_f = k_o \cdot exp(-r\sigma_3)$, where k_o is the permeability at zero minor principle stress $\sigma_3 = 0$ and γ is a parameter characterizing the dilatability of the interconnected cracks. When the fractured claystone is recompacted with increasing σ_3 to $(\sigma_1 - \sigma_3) < \sigma_R$, the fracture permeability tends to decrease following the cubic law, where $\Delta\varepsilon_R = |\varepsilon_F - \varepsilon_v|$ represents the residual void in the fractures, ε_F is the maximum dilatancy at the final damaged state and $D = k_f/\varepsilon_F^3$ is a parameter characterising the final damaged state. As the residual fracture void tends to zero, $\Delta\varepsilon_R \rightarrow 0$, the fracture permeability disappears.

3 SIMULATION OF LABORATORY EXPERIMENTS

3.1 Parameters

The model parameters were determined from the GRS's laboratory experiments on the COX claystone. In the calculations, the Biot effective stress concept is adopted: $p^b = p^t - Bp^l$, where p^t is the total mean stress, p^l is the porewater pressure, p^b is the effective stress, and B is a parameter. The mechanical parameters used for modelling are summarized in table 1.

Table 1 Mechanical parameters for the COX claystone

Biot stress parameter	$p^b = p - Bp^l$: $B = 0.6$
Elastic moduli	E = 6.3 GPa, ν = 0.2, K_s = 1E7 MPa
Yield parameters	$c = 6$ MPa, $\varphi = 26°$, $\varpi = 0.1$, $\theta = 25°$
Hardening-softening parameters	$\beta^{ini} = \varphi_{ini}/\varphi_{peak} = 0.42$, $\alpha_{hard} = 0.0035$ $\beta^{res} = \varphi_{ires}/\varphi_{peak} = 0.8$, $\alpha_{soft} = 0.07$ $\xi_1 = 0.001\sigma_3 + 0.001$, $\xi_2 = 0.001\sigma_3 + 0.002$, $\xi_3 = 0.001\sigma_3 + 0.012$
Creep parameters	σ_s = 2 MPa, $\varepsilon_{eq}^{vp} = 0$, γ = 4.5·10^{-9} d^{-1}, n = 2.5, m = 530

The parameters associated to the permeability model (Eq. 5) were estimated: k_c = 10^{-20} m^2, k_o = 3·10^{-13} m^2, γ = 1.9 MPa^{-1}, and D varies in a range of 7·10^{-10} m^2 to 1·10^{-7} m^2 depending on the damage intensity of the claystone.

3.2 Simulation of the short-term deformation

Figure 3 shows the modelling results for a series of triaxial compression tests on the COX samples. It is obvious that the short-term elastoplastic response with hardening and softening effects can be reasonably represented by the model. The model shows the continual volumetric compression until the peak stress followed by dilatancy with softening. There are some quantitative discrepancies between the calculated and measured volumetric strains. It is also to be pointed out that the equivalent plastic strain parameters ξ_1, ξ_2, ξ_3 are not constant but vary with the minor confining stress σ_3. This is due to the increased ductility of the claystone at high confining stresses. In the calculations, the plastic strain parameters are preliminarily assumed to be linearly related with the confining stress as shown in table 1 and figure 4. This assumption provides the sound modelling results. These equations shall be implemented in the code.

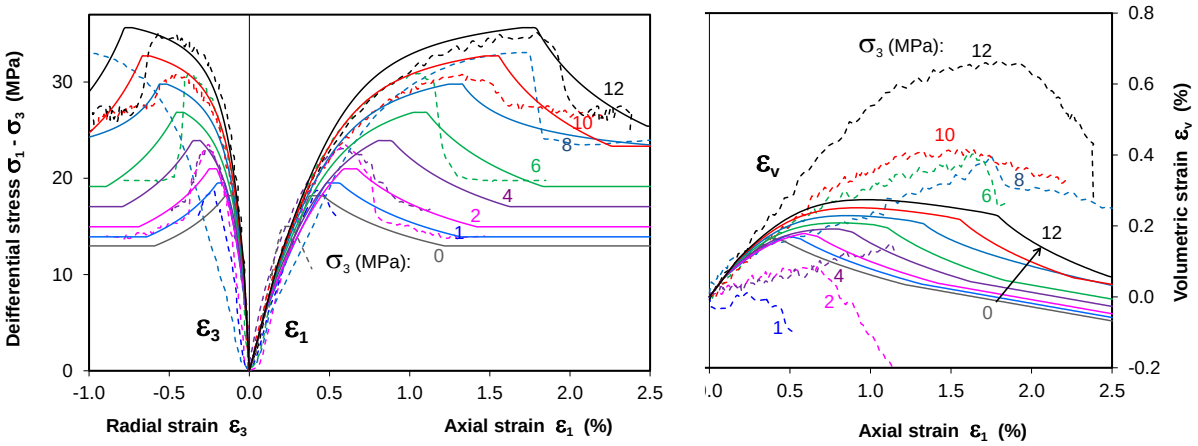

Figure 3 Modelling results of the short-term deformation of the COX claystone during triaxial loading

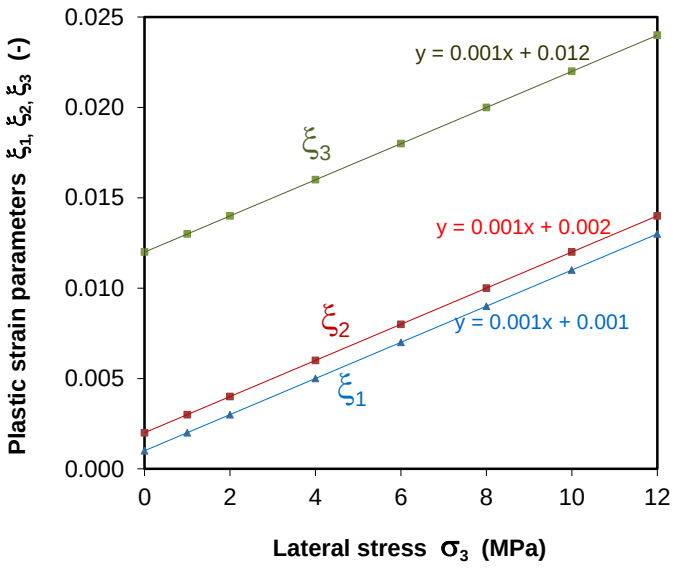

Figure 4 Plastic strain parameters as function of the minor confining stress

3.3 Simulation of the long-term deformation

Figure 5 shows an example of the modelling results for a triaxial creep test on a COX sample under very low deviatoric stresses. The model curves are close to the measured data. But the short transient creep stage cannot be well matched by the model, indicating that the given value of the strain hardening parameter m = 530 in Eq. (4) is too large. This is however not of importance for prediction of the long-term deformation of the clay host rock during the repository post-closure phase over hundreds of thousands of years.

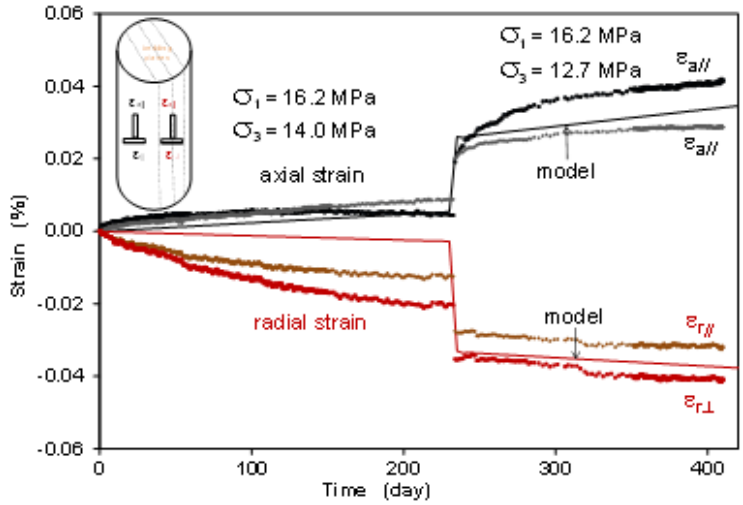

Figure 5 Modelling results of the creep of the COX claystone under low deviatoric stresses

3.4 Simulation of the fracturing-induced permeability

Figure 6 shows an example of the permeability modelling results for a triaxial compression test on a COX sample under loading. The implementation in the model is preliminary, but the figure already shows the progressive damage induced in the sample from the peak strength to the residual strength, which leads to a rapid increase in the permeability.

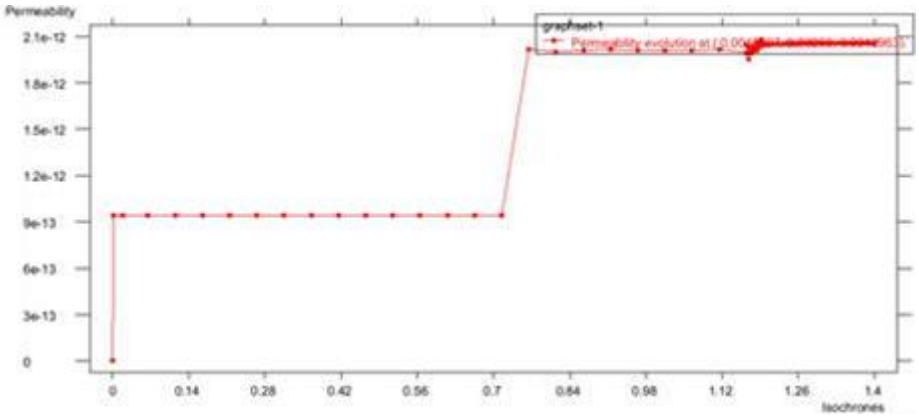

Figure 6 Modelling results of the permeability of the COX claystone during triaxial loading

REFERENCES

Ruiz, D.F., Vaunat, J., Gens, A., Manica, M., Pasteau, A. (2015): Insights into the response of a gallery sealing over the entire life of a deep repository, The 6th International Clay Conference – Clays in Natural & Engineered Barriers for Radioactive Waste Confinement, March 23-26, 2015, Brussels.

Zhang, C.L. (2015): Deformation of Clay Rock under THM Conditions, Journal of Geomechanics and Tunnelling 8 (2015), No. 5, 426-435.

Zhang, C.L. (2016): The Stress-Strain-Permeability Behaviour of Clay Rock during Damage and Recompaction, Journal of Rock Mechanics and Geotechnical Engineering 8 (2016), 16-26.

HYDROMECHANICAL SIMULATION OF A DRIFT EXCAVATED IN THE CALLOVO-OXFORDIAN ARGILITE

Mánica M.[*], Gens A.[*], Vaunat J.[*] and Ruiz D.[*]

[*] Department of Civil and Environmental Engineering
Technical University of Catalonia (UPC)
Campus Nord UPC, 08034 Barcelona, Spain
e-mail: miguel.angel.manica@estudiant.upc.edu

Key words: HM coupled analysis, Elasto-plasticity, argillaceous rocks.

Abstract. *A constitutive model is presented for the simulation of argillaceous rocks. It was developed within the framework of elasto-plasticity and includes a number of features that were considered essential for a satisfactory description of their behaviour. The model has been applied to the coupled hydromechanical simulation of an underground excavation. Results were compared with in situ measurements, where a reasonable agreement was observed.*

1 INTRODUCTION

Argillaceous rocks and stiff clay formations have shown great potential as possible geological host medium for radioactive waste. These materials have low permeability, significant retardation properties, no economic value (with the exception of gas or oil shales) and they often exhibit a significant capacity of self-sealing of fractures. In this context, the French national radioactive waste management agency (Andra) started in 2000 the construction of the Meuse/Haute-Marne (MHM) Underground Research Laboratory (URL), excavated in the Callovo-Oxfordian argillite (COx), to demonstrate the feasibility of these materials to host a radioactive waste repository. Several *in situ* experiments have been performed, including heavily instrumented experimental excavations, in many cases accompanied with comprehensive laboratory testing programs. These studies have revealed, among others, the following features regarding the mechanical behavior of the COx: Strength and stiffness anisotropy; significant nonlinearities and plastic strains prior to peak strength; a quasi-brittle behavior at the *in situ* stress range, with a significant strength loss in the softening branch of the stress-strain curve; creep deformations with increasing rates for higher deviatoric stresses.

In this paper, a constitutive model is described aimed to reproduce the main features of behavior of the COx mentioned above. The developed constitutive model has then been applied to the simulation of one of the experimental excavations in the MHM URL. Results were compared with *in situ* measurements, which allowed us to evaluate the performance of the numerical approach presented herein.

2 CONSTITUTIVE MODEL

The model comprises two main deformation mechanisms (for a perfectly drained hypothetical condition): a time-independent response related to stress changes and a time-dependent response occurring under constant stress. However, the hydro-mechanical coupling will give rise to consolidation and in this case both mechanisms will be time-dependent.

A generalized effective stress expression has been adopted here:

$$\boldsymbol{\sigma}' = \boldsymbol{\sigma} + Se\, s\, B\, \mathbf{I} \tag{1}$$

where $\boldsymbol{\sigma}'$ is the effective stress tensor, $\boldsymbol{\sigma}$ is the total stress tensor, Se is the equivalent degree of saturation, s is suction, B is Biot's coefficient and $\mathbf{I}$ is the identity tensor. In the following, the term "stress" always denotes effective stress.

2.1 Time-independent response

The time-independent response is described within the framework of elasto-plasticity. Under low deviatoric stresses the response is linear elastic, but characterized through a transverse isotropic form of the Hook's law. For higher deviatoric stresses plastic deformations can take place. An initial, a peak and a residual yield limits are considered. The first one defines a surface in the stress space that separates the elastic and plastic regions, but further loading can be sustained by the material. This is physically related to the development and growth of microcracks, modelled through hardening plasticity. On the other hand, the peak limit represents the maximum strength of the material and states beyond this boundary are not allowed. From this point strength is gradually reduced to its residual value, the latter being related to the coalescence of microcracks into macrocracks, modelled through softening plasticity. The Mohr-Coulomb criterion is used for the initial, peak and residual limits, which in terms of commonly employed stress invariants reads:

$$f = (\cos\theta + \sin\theta \sin\phi / \sqrt{3})\, J - \sin\phi\, (p + c \cot\phi) \tag{2}$$

where $p\ J\ \theta$ are stress invariants, ϕ is the friction angle and c is the cohesion.

The initial, peak and residual limits are obtained with Eq. (2), by using the corresponding strength parameters (ϕ and c). The evolution of the yield surface within these limits is considered through non-linear isotropic hardening/softening, driven by the evolution of the strength parameters. A scalar measure of the plastic strains (Eq. 3) has been chosen as the state variable controlling this evolution.

$$\varepsilon^{p}_{eq} = [(2/3)\, \boldsymbol{\varepsilon}^{p} : \boldsymbol{\varepsilon}^{p}]^{1/2} \tag{3}$$

The friction angle varies in a piecewise manner as shown in Fig. 1.

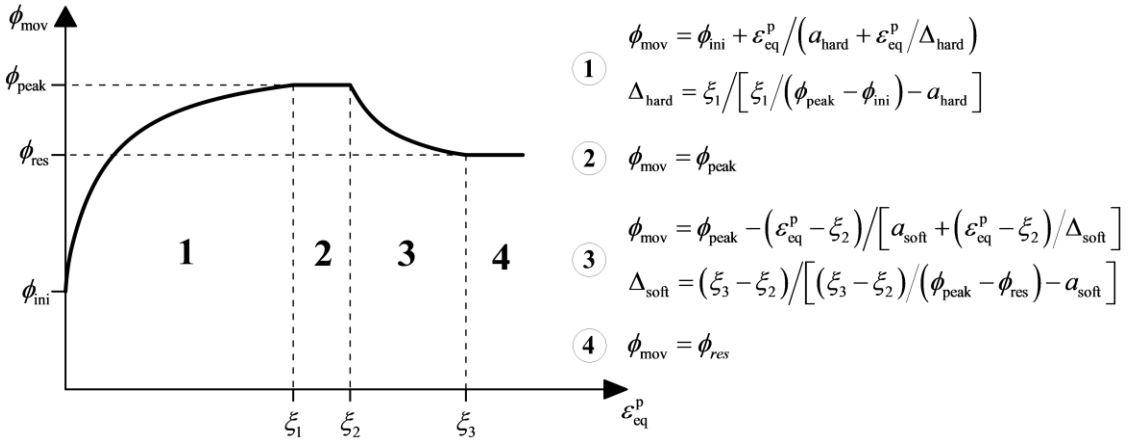

Figure 1: Friction angle evolution during hardening/softening

Cohesion evolves in parallel with the friction angle according to:

$$c_{mov} = c_{peak} \cot \phi_{ini} \tan \phi_{mov} \tag{4}$$

A non-associated flow rule is adopted in the model. Rather than deriving a specific function for the plastic potential, the flow rule is directly obtained from the yield criterion in the following way:

$$\partial g / \partial \boldsymbol{\sigma} = \omega \, (\partial f / \partial p) \, (\partial p / \partial \boldsymbol{\sigma}) + (\partial f / \partial J) \, (\partial J / \partial \boldsymbol{\sigma}) + (\partial f / \partial \theta) \, (\partial \theta / \partial \boldsymbol{\sigma}) \tag{5}$$

where g is the plastic potential and ω is a constant that controls the volumetric component of plastic deformations.

The model has been extended to consider strength cross-anisotropy through a non-uniform scaling of the stress tensor. This extension is obtained by replacing p J θ in Eq. (2) by p^{ani} J^{ani} θ^{ani} respectively. These variables are invariants with its usual definition, but calculated from the anisotropic stress tensor ($\boldsymbol{\sigma}^{ani}$). For the definition of this tensor we consider an additional local coordinate system oriented with respect to the anisotropic characteristics of the material (Fig. 2).

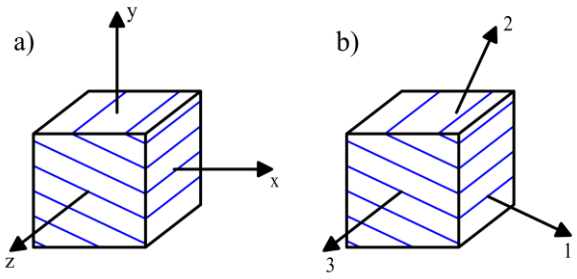

Figure 2: (a) Global and (b) local coordinate systems.

Stresses with respect to the local system ($\boldsymbol{\sigma}^{r}$) are evaluated by applying usual rotation of axes. $\boldsymbol{\sigma}^{ani}$ is then obtained through the non-uniform scaling of $\boldsymbol{\sigma}^{r}$. Taking into account the restrictions imposed by the assumption of cross-anisotropy, the following form is proposed for $\boldsymbol{\sigma}^{ani}$:

$$\boldsymbol{\sigma}^{ani} = \begin{bmatrix} \dfrac{\sigma_{11}^{r}}{c_N} & c_S \sigma_{12}^{r} & \sigma_{13}^{r} \\ c_S \sigma_{12}^{r} & c_N \sigma_{22}^{r} & c_S \sigma_{23}^{r} \\ \sigma_{13}^{r} & c_S \sigma_{23}^{r} & \dfrac{\sigma_{33}^{r}}{c_N} \end{bmatrix} \tag{6}$$

where c_N and c_S are the normal and shear scaling factors respectively. Details about the physical meaning of the anisotropy parameters, their effects and regarding the implementation of this approach are given in Mánica *et al.*[i]

2.2 Time-dependent response

An additional mechanism is considered for the time-dependent response, characterized by a modified form of the Lemaitre's law. The total strain increment is decomposed as the sum of the two mechanisms:

$$d\boldsymbol{\varepsilon} = d\boldsymbol{\varepsilon}^{ep} + d\boldsymbol{\varepsilon}^{vp} = d\boldsymbol{\varepsilon}^{ep} + dt \, \dot{\boldsymbol{\varepsilon}}^{vp} \tag{7}$$

where $d\boldsymbol{\varepsilon}$ is the total strain increment, $d\boldsymbol{\varepsilon}^{ep}$ is the elastoplastic strain increment (time-

independent response), d$\boldsymbol{\varepsilon}^{vp}$ is the visco-plastic strain increment (time-dependent response), dt is the time increment and $\dot{\boldsymbol{\varepsilon}}^{vp}$ is the visco-plastic strain rate tensor.

It is assumed that visco-plastic deformations are mainly caused by deviatoric stresses, with strain rates given by:

$$\dot{\boldsymbol{\varepsilon}}^{vp} = \left(2\dot{\varepsilon}^{vp}/3q\right)\mathbf{s} \tag{8a}$$

$$q = \left[\left(3/2\right)\left(\mathbf{s}:\mathbf{s}\right)\right]^{1/2} \tag{8b}$$

$$\dot{\varepsilon}^{vp} = \gamma\left(q-\sigma_s\right)^n\left(1-\varepsilon_{eq}^{vp}\right)^m \tag{8c}$$

where γ is a viscosity parameter, σ_s is a threshold from which visco-plastic strain are activated, n and m are material constants and ε_{eq}^{vp} is the state variable of the time dependent response given by:

$$\varepsilon_{eq}^{vp} = \int_0^t \left(\frac{2}{3}\dot{\boldsymbol{\varepsilon}}^{vp}:\dot{\boldsymbol{\varepsilon}}^{vp}\right)^{1/2} \mathrm{d}t \tag{9}$$

3 APLICATION TO THE EXCAVATED DRIFT

The described constitutive model has been applied to the simulation of the GCS drift, excavated at the -490 m level of the MHM URL (Fig. 3a). The drift alignment is parallel to the major principal stress, and stresses in the plane orthogonal to the tunnel axis are reported as nearly isotropic. However, the damaged zone extends significantly more in the horizontal direction (Fig. 3b). Larger horizontal convergences are also observed, that suggest strong anisotropic characteristics of the rock mass. More details on the GCS drift are given in Armand *et al.*[ii]

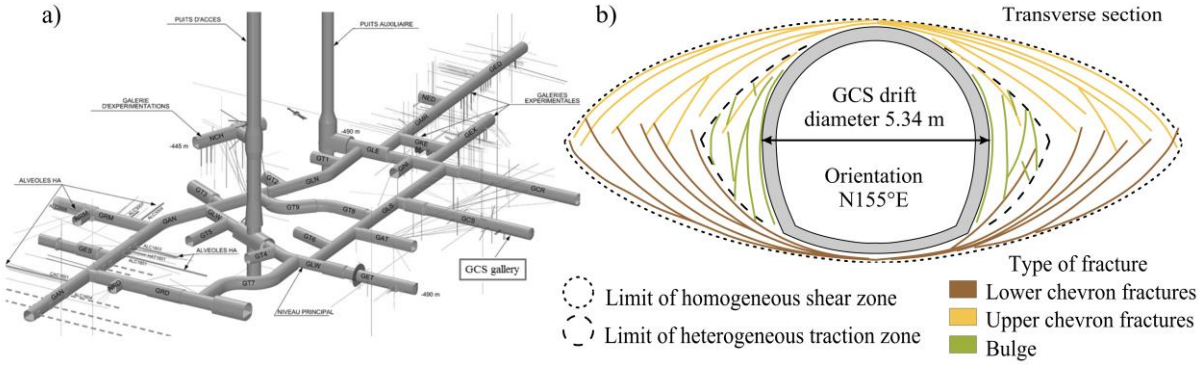

Figure 3: (a) Location of the GCS drift in the MHM URL and (b) extension of the damaged zone (Armand *et al.*[ii]).

3.1 Parameter calibration

Parameters employed in the drift simulation were calibrated by modelling triaxial and creep test (also under triaxial loading) performed on COx samples. Fig. 4a shows the obtained stress-strain curves from the simulated triaxial test, for confinement pressures of 6 and 12 MPa, together with the laboratory results. Fig. 4b shows the results of the creep test performed at a confinement pressure of 12 MPa, for different ratios between the applied and maximum deviatoric stresses. In both cases the main characteristics are reasonably captured.

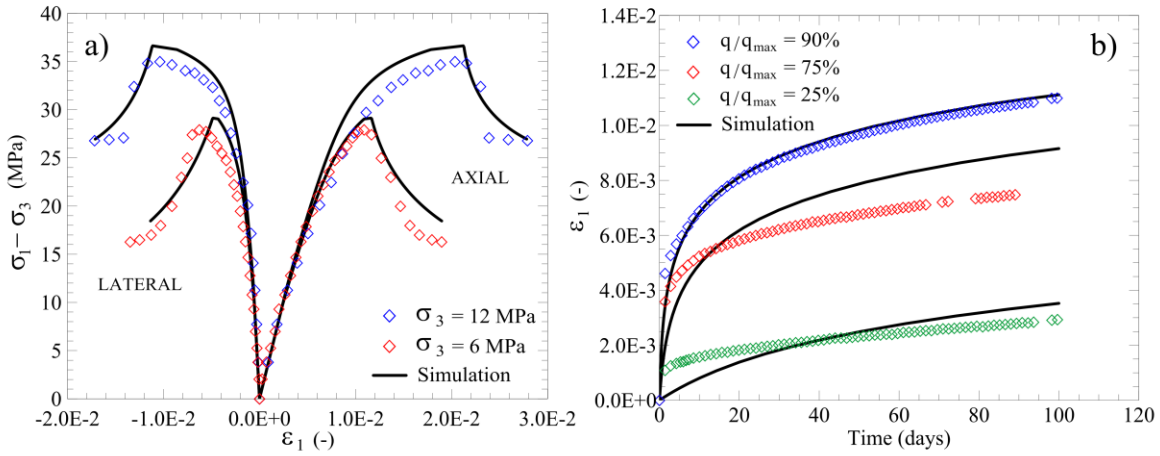

Figure 4: (a) Triaxial and (b) creep test; observations and model results

3.2 Main features of the numerical model

The coupled hydromechanical formulation employed herein to the solution of the analyzed boundary value problem is a particular case of the general formulation presented in Olivella *et al.*[iii] Plane strain conditions are assumed and the stress gradient due to gravity was neglected. The mesh and main boundary conditions (BC) are illustrated in Fig. 5a. Excavation is simulated by the deconfinement curve shown in Fig 5b. The deconfinement ratio is defined as the relationship between the surface stress applied to the boundary and the value in equilibrium with the initial stress conditions. In this way, the three-dimensional nature of the problem is considered in an approximate manner.

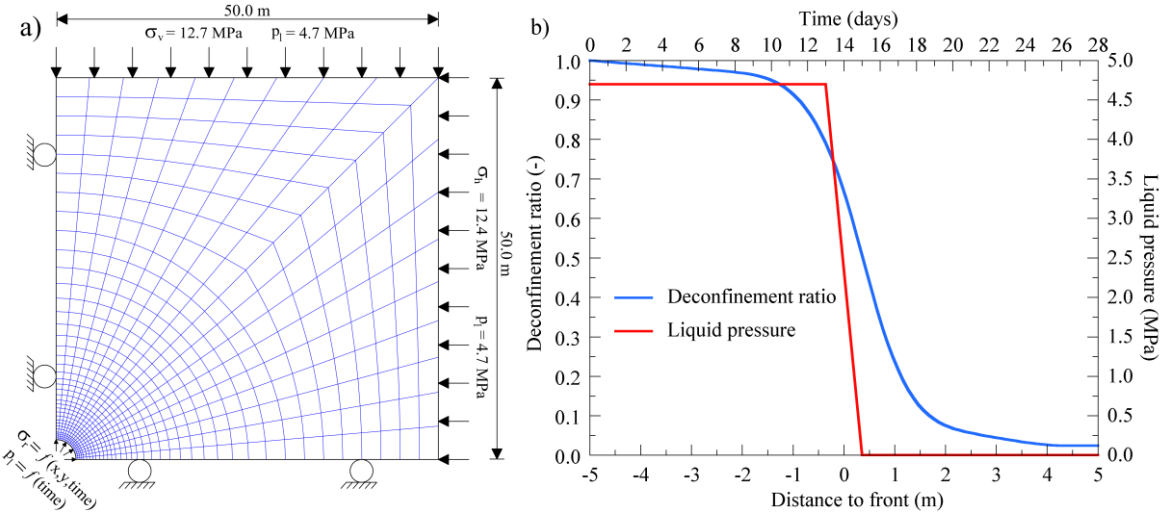

Figure 5: (a) Finite element mesh, main BC and (b) time dependency of BC in the excavation wall

3.3 Obtained results

Some selected results are depicted in Fig. 6. A contour plot of cumulative values of the plastic multiplier are shown in Fig. 6a, which is an excellent means to observe the extension and configuration of the obtained plastic zone. Despite the initial isotropic stress state in the analysis section, the plastic zone configuration extends significantly more in the horizontal

direction, as it is observed in the field (Fig. 3b). Fig. 6b shows the displacements recorded by an extensometer installed along the horizontal direction, together with the model results. The largest displacements correspond to a measurement point close to the excavation wall, which is nicely predicted by the simulation. In the remaining locations somewhat larger differences are observed, although the general trend of behavior is reasonably capture.

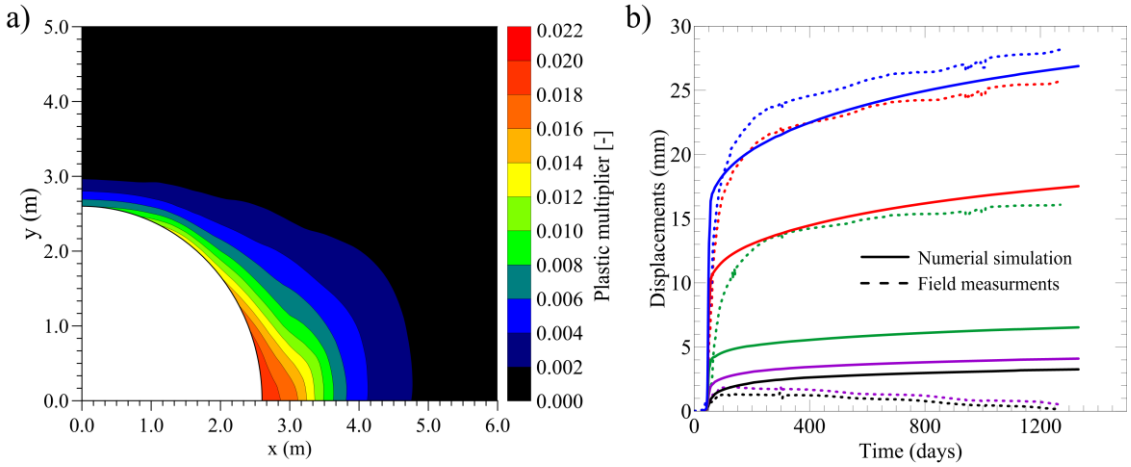

Figure 6: (a) Obtained configuration of the damaged zone and (b) horizontal displacements at different locations

4 CONCLUDING REMARKS

This paper presents a constitutive model for argillaceous rocks that includes a number of features that are relevant for a satisfactory description of the behavior of these materials. The model has been applied, via a suitable hydromechanical formulation, to the simulation of an underground excavation in the MHM URL. The main trends of behavior where reasonably captured, especially the capability of the model to reproduced unsymmetrical plastic zone configurations, in the presences of an isotropic stress state, by considering the anisotropy characteristics of the rock mass.

ACKNOWLEDGEMENTS

The funding and assistance of Andra to the work presented is gratefully acknowledged.

REFERENCES

[i] Mánica M., Gens A., Vaunat J., Ruiz D., (in press). A cross-anisotropic formulation for elasto-plastic models. Géotechnique Letters.

[ii] Armand G., Noiret A., Zghondi J., Seyedi D.M., 2013. Short- and long-term behaviors of drifts in the Callovo-Oxfordian claystone at the Meuse/Haute-Marne Underground Research Laboratory. Journal of Rock Mechanics and Geotechnical Engineering, 5, 221:230.

[iii] Olivella, S., J. Carrera, A. Gens, E. E. Alonso, 1994. Non-isothermal Multiphase Flow of Brine and Gas through Saline media. Transport in Porous Media, 15, 271:293.

MODELLING THE TIME-DEPENDENT MECHANICAL BEHAVIOR OF CONCRETE BASED SEALING MATERIAL IN ROCK SALT RELATED TO THE DOPAS-PROJECT

–

APPLICABILITY ASSESSMENT OF THE "ARGILLITE-/COMPOSITE-MODEL"-APPROACH

M. Middelhoff [1], O. Czaikowski [2]

[1] Institute of Disposal Research (IELF)
Clausthal University of Technology
Adolph-Roemer-Straße 2a, 38678 Clausthal-Zellerfeld, Germany
E-Mail: Marvin.Middelhoff@tu-clausthal.de, Web Page: https://www.ielf.tu-clausthal.de/de/

[2] Gesellschaft für Anlagen- und Reaktorsicherheit (GRS) gGmbH
Theodor-Heuss-Straße 4, 38122 Braunschweig, Germany
E-Mail: Oliver.Czaikowski@grs.de, Web Page: http://www.grs.de/

Key words: Sealing materials, rock salt, salt concrete, modelling, DOPAS

Abstract: *In the former German concept, rock salt was the favorite host rock to dispose heat-generating radioactive waste. To assure the integrity of the complete repository system after closure, shafts and drifts have to be sealed. In the context of the DOPAS project GRS performed a laboratory test program and numerical simulations to investigate the properties of concrete based sealing materials. The test program and the numerical simulations mainly focused on salt concrete. This paper assesses the applicability of the unpublished "Argillite-/Composite-Model" approach implemented in CODE_BRIGHT and illustrates the reason why it can be an alternative approach for simulating the long-term mechanical behavior of concrete based sealing materials in rock salt in future.*

1 INTRODUCTION

The German safety requirements for a repository of heat-generating nuclear waste [i] comprise several safety principles, the most important ones being (a) the Radionuclides and other contaminants in the waste must be concentrated and contained in a containment-providing rock zone and thus be isolated from the biosphere as long as possible. And (b) waste disposal must ensure that release of radionuclides from the repository enhances only insignificantly the risks resulting from natural radiation exposure.

On behalf of the Federal Ministry for Economic Affairs and Energy (BMWi), the national funding organisation for R&D work related to radioactive waste management in Germany, GRS is investigating sealing and backfilling materials potentially utilised in salt and clay formations.

By constructing a repository, shafts and drifts penetrate the integrity of the host rock and could develop potential pathways, relevant for the migration of radionuclides. Therefore, engineered barrier systems have been developed for sealing the shafts and galleries. All systems include the utilization of concrete based sealing materials. Beside other materials like sorel concrete, salt concrete is a prospective used material, which is composed of salt grains, cement and brine.

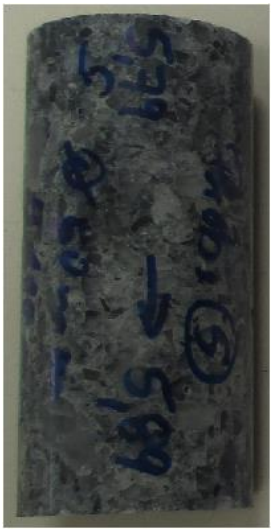

Fig. 1: Example of a salt concrete specimen used by GRS in the laboratory tests

To investigate the time-dependent mechanical behavior on salt concrete specimen, GRS carried out a comprehensive laboratory test program, followed by numerical simulations by using CODE_BRIGHT within the scope of the European project DOPAS (Full scale Demonstration of Plugs and Seals) under WP 3 on "Design and technical construction feasibility of the plugs and seals" and WP 5 "Performance assessment of plugs and seals system" [ii]. Financial support is given 50 % by the DOPAS project and co-funded by BMWi.

This paper concentrates on a recently performed experiment and the calibration simulations, which base upon previously gained results. To simulate the time-dependent deformation behavior of salt concrete, GRS has successfully been using a combination of constitutive laws related to the behavior of rock salt (Hooke/ Dislocation Creep/ Viscoplasticity (H/DC/VP)) since 2015. Although simulations using the combination of H/DC/VP obtain realistic results, GRS is convinced, that the "Argillite-/Composite-Model"-approach (AM-approach) implemented in CODE_BRIGHT might even reveal more precise results due to the composition and structure of salt concrete.

The objective of this paper is to assess the applicability of the unpublished AM-approach and to illustrate the results of the first calibration work within the numerical simulations.

2 RECENTLY PERFORMED EXPERIMENTS AND SIMULATIONS

In the middle of 2015, GRS started executing a triaxial-compression-creep test (TCc-test) with concrete based sealing materials (Salt concrete and Sorel concrete) to review and compare the previously obtained results of previous test results. The salt concrete specimens were extracted from a drift sealing element in a former salt mine. The drift sealing element has been affected by convergence processes for more than 10 years. Now the test has been lasting for more than 8 months and the results have been accompanied by numerical simulations using a parameter set based upon H/DC/VP [ii].

2.1 Results of recently performed experiments

In a special apparatus for triaxial testing of 5 cylindrical samples simultaneously, 2 previously damaged salt concrete samples and 2 sorel concrete have been tested. First the specimens have been subjected to hydrostatic stress, in the second stage the deviatoric stress has been increased to 8 MPa and finally creep deformations should be induced by an increase to 20 MPa. The measurement results of the TCc-test are shown in Fig. 2.

The recent TCc-test revealed similar results in comparison to the previously performed tests. Beside the initial mean strain of specimen "Salt concrete (1068)" both specimens show similar deformation behavior in the long term. Subjecting the samples to deviatoric stresses below 20 MPa, the elastic behavior of the salt concrete becomes visible. A clear creep behavior of the salt concrete is just detectible during deviatoric stress above 20 MPa (compare "Salt concrete (1069)" in Fig. 3).

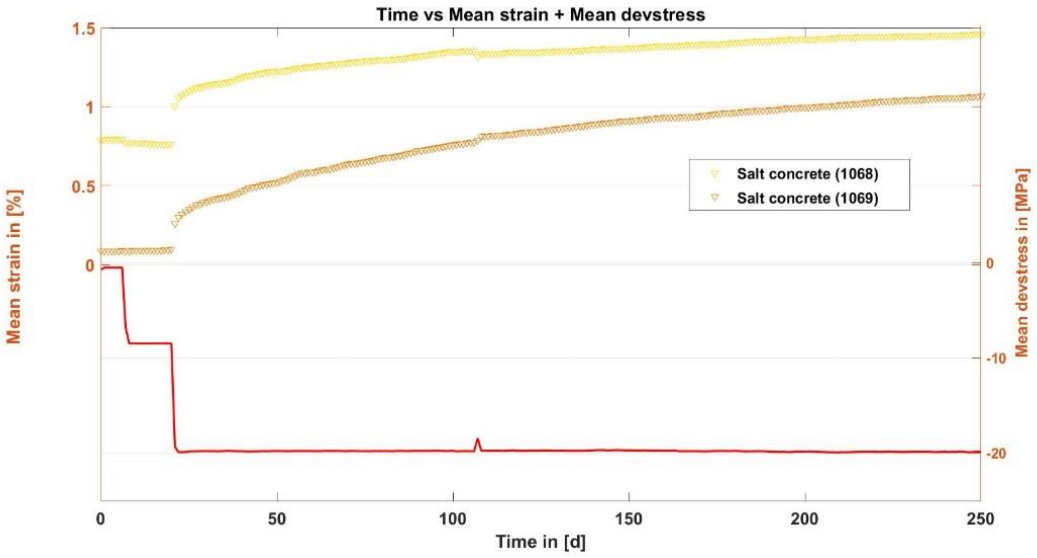

Fig. 2: Results of the TCc-test: Illustration of the strain progress over time with regard to different deviatoric stress levels

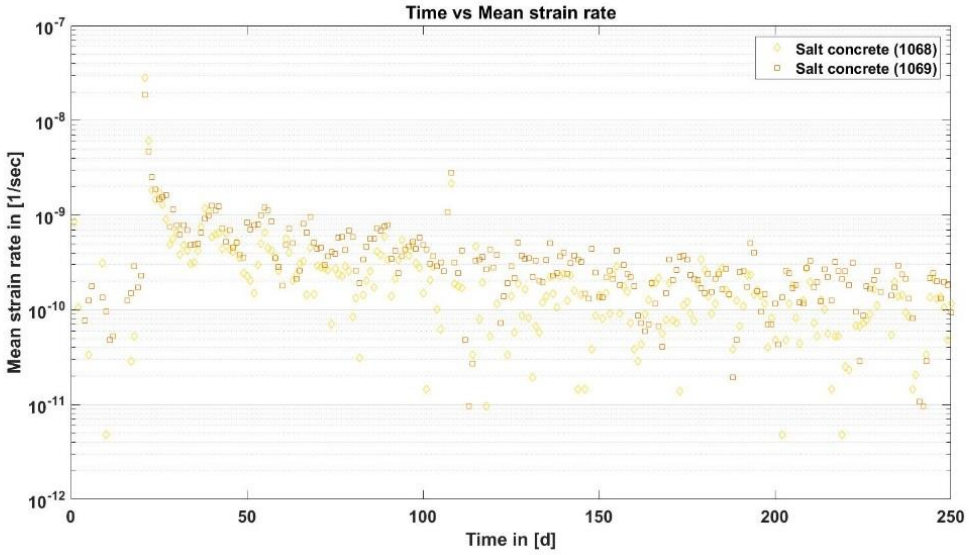

Fig. 3: Results of the TCc-test: Illustration of the strain rate over the time

2.2 Recently performed simulations - (Applicability assessment of the Lemaitre's model)

Due to the composition and structure of the concrete based sealing materials, it might be possible, that the implemented AM-approach in CODE_BRIGHT seems to be an alternative approach to simulate the time-dependent mechanical behavior of these materials even more precisely than the H/DC/VP-approach. The AM-approach generally includes constitutive laws handling the material behavior of a solid phase matrix, the material behavior of bond structures and their interactions. Actually this model-approach is used for simulating soft rocks, like argillaceous rock, but moreover it seems to be applicable to model concrete, respectively salt and sorel concrete.

Nevertheless, one issue emerged concerning the creep behavior of the salt concrete in previous considerations. The AM-approach does not include a particular creep law for rock salt, like the DC and VP. It offers the Lemaitre law as an opportunity, but it has to be proven, whether the modified Lemaitre law is able to simulate creep behavior of salt concrete.

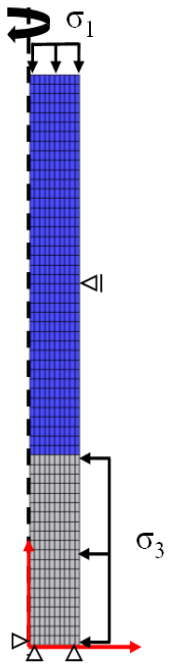

Fig. 4: 2D-Model

As it is shown in Fig. 4, a 2D-model was developed similar to the model, which was used in the previous simulations [ii]. Due to the symmetry of the sample and the piston, the model has been constructed symmetrically around the y-axis. The upper part represents the steel piston. The lower part colored in grey illustrates the specimen.

To avoid any motion at the base of the specimen, displacements have been prescribed by nodal forces in x- and y-direction. This conditions are not in accordance with the real conditions, but it made the solution of the numerical problem simpler. Motions in x-direction have been prescribed at the sides of the steel piston as well. Finally, to represent the axial and radial stresses of the sample, boundary stresses have been applied on the line affecting the side of the sample. The initial conditions have remained the same as they were used in the previous simulations [ii].

The mesh was generated by using 600 quadratic elements and 671 nodes. The stages of 3 different deviatoric stress levels (Phase 1: σ_{dev} = 0 MPa; Phase 2: σ_{dev} = 8 MPa; Phase 3: σ_{dev} = 20 MPa) have been modelled close to the real progress of the experiment. However, the phases of loading have been simulated separately.

Tab.1 illustrates which parameters are necessary to model the mechanical behavior of salt concrete. Due to the fact that this simulation is a preliminary one, any effects concerning hardening, softening, viscoplasticity, bonding, couplings between bonds and matrix have been neglected. The equations (1) to (3) describe the theoretical background.

Argillite Matrix	E^M_h * [MPa]	ν^M_h [MPa]	
	25000	0.18	
Argillite Plastic dev.	σ_s [MPa]	γ [Day^{-1}]	m [-]
	12	5e-4	390/ 580

Tab. 1: Used material parameter set for simulating the TCc-test (AM-approach)

The part "Argillite Plastic dev." includes the modified creep law of Lemaitre (compare (2.3)). σ_s represents a threshold parameter that controls the start of creep deformations.

$$d\boldsymbol{\varepsilon} = d\boldsymbol{\varepsilon}^{\mathbf{ep}} + d\boldsymbol{\varepsilon}^{\mathbf{vp}} = d\boldsymbol{\varepsilon}^{\mathbf{ep}} + \Delta t(\dot{\boldsymbol{\varepsilon}}^{\mathbf{vp}}) \tag{1}$$

$$\dot{\boldsymbol{\varepsilon}}^{\mathbf{vp}} = \frac{2}{3}\frac{\dot{\varepsilon}^{vp}}{q}\mathbf{s} \tag{2.1}$$

$$q = \left(\frac{3}{2}\mathbf{s}:\mathbf{s}\right)^{1/2} \tag{2.2}$$

$$\dot{\varepsilon}^{vp} = \gamma(q - \sigma_s)^n \left(1 - \varepsilon_{eq}^{vp}\right)^m \tag{2.3}$$

$$\varepsilon_{eq}^{vp} = \int_0^t \left(\frac{2}{3}\dot{\boldsymbol{\varepsilon}}^{\mathbf{vp}}:\dot{\boldsymbol{\varepsilon}}^{\mathbf{vp}}\right)^{1/2} dt \tag{3}$$

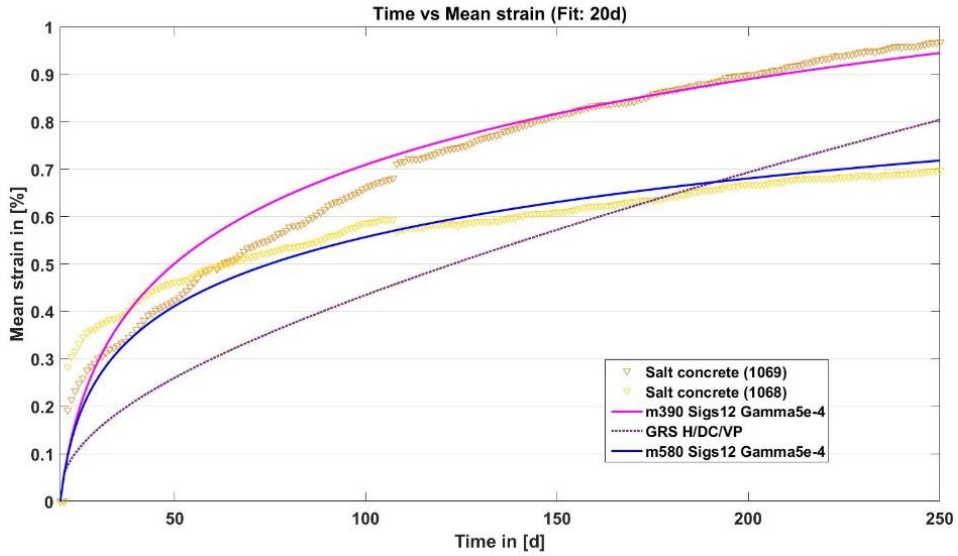

Fig. 5: Results of the calibration work focusing on the phase of deviatoric stress above 20 MPa: The magenta and the blue curves show the calibrated AM-parameter sets - the purple one represents the H/DC/VP approach

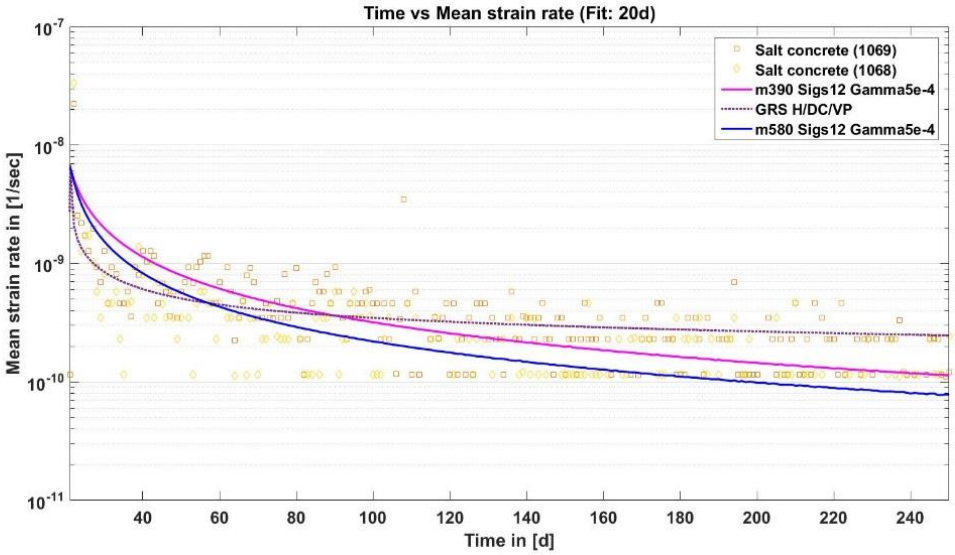

Fig. 6: Results of the calibration work focusing on the phase of deviatoric stress at 20 MPa

The modified Lemaitre law included in the AM-approach obtains a proper approximation concerning the creep behavior of the salt concrete, which is visible in Fig. 5. Nevertheless, in comparison to the AM-approach, the H/DC/VP-parameter set is able to describe the phase of stationary creep more precisely. Fig. 6 reveals, that both approaches achieve similar strain rates in comparison to the experiments, but the strain rates of the AM-approach tend to become too small at the end.

3 CONCLUSION

The numerical simulation of the performed TCc-test should serve the purpose to assess the applicability of the modified Lemaitre law included in the unpublished AM-model with focus on the creep behavior of concrete based sealing materials in rock salt. After performing calibration work, material parameter sets were developed, which are able to simulate creep behavior, similar to the creep behavior of salt concrete. So it can be summarized, that this AM-approach is applicable to simulate the time-dependent mechanical behavior of concrete based sealing material in rock salt.

Future work should concentrate on finding one general parameter set, which covers the short- as well as the long-term mechanical deformation behavior, especially stationary and tertiary creep, as well as the matrix-bond-coupling.

4 ACKNOWLEDGEMENT

The authors gratefully acknowledge the funding of the European Commission under FP7 framework program, contract no. FP-7323273 the DOPAS project and the funding received by the Federal Ministry of Economics and Energy (BMWi), represented by the Project Management Agency Karlsruhe (PTKA-WTE), contract no. 02E11132.

5 REFERENCES

[i]: BMU: Sicherheitsanforderungen an die Endlagerung wärmeentwickelnder radioaktiver Abfälle. Stand 30. September 2010, Bundesministerium für Umwelt, Naturschutz und Reaktorsicherheit (2010)

[ii]: Czaikowski, O., Dittrich, J., Hertes, U., Jantschik, K., Wieczorek, K., Zehle, B.: Full scale demonstration of plugs and seals (DOPAS), Deliverable D3.31. Final technical report on ELSA related testing on mechanical-hydraulical behaviour - LASA, Gesellschaft für Anlagen- und Reaktorsicherheit (GRS) gGmbH, GRS-A-Bericht 3851, February 2016

[iii]: CODE_BRIGHT, 2002. A 3D program for thermos-hydro-mechanical analysis in geological media. Users guide

VERIFICATION OF THE HEAT FLOW DISSIPATION CALCULATION IN NUCLEAR SPENT FUEL REPOSITORY

X. Pintado*

* B+TECH Oy; Laulukuja 4 00420 Helsinki, Finland
Email: xavier.pintado@btech.fi

Key words: TH model, thermal model, KBS-3H, KBS-3V

Abstract. *There are many design requirements that must be followed for the disposal of spent nuclear fuel. For example, the maximum temperature is limited in order to avoid harmful mineralogical changes in the bentonite, the main component of the EBS (Engineered Barrier System). This paper presents a verification of the thermal results obtained from 2-D calculations solving only the energy balance equation combined with the analytical solution used for the definition of the distances between canisters and the results obtained from 3-D calculations solving the energy mass balance equation as well. The KBS-3H alternative has almost the same results in both calculations but KBS-3V alternative presents some differences which could be due to the weakness of the 2-D approximation. In any case, the design method is on the safety side because the temperatures calculated are the highest.*

1 INTRODUCTION

The final spent nuclear fuel disposal is based on the use of multiple release barriers, which ensures that the spent nuclear fuel cannot be released into organic nature or become accessible to humans. The spent nuclear fuel will be encapsulated in metal canisters installed in individual vertical holes (KBS-3V alternative [1]) or in horizontal drifts with tens of canisters at the same drift (KBS-3H alternative [2]). The canisters will be surrounded by bentonite blocks (buffer). The maximum temperature allowed is 100°C in order to avoid harmful mineralogical changes, like the change from montmorillonite to illite and the loss of the swelling capacity of the bentonite. In order to have a safety margin in the design, the maximum temperature calculated cannot be more than 95°C. In this case, the distance between axis canisters for the nuclear spent fuel generated in the reactors 1 and 2 of the Olkiluoto nuclear power plant is 8.9 m [3] in KBS-3V and the distance between the center of the canisters in KBS-3H is 9.0 m [4].

2 MODELS DESCRIPTION

The canisters in KBS-3V alternative are surrounded by ring blocks and there is an air gap of 10 mm thickness (nicknamed “inner gap”) between them. There are also disc blocks on top and at the bottom of the canister. There is a second gap between the blocks and the host rock. This gap has 50 mm thickness and will be filled with pellets (Figure 1a). The KBS-3H emplaces the canisters inside a perforated metal shell. There are rings and discs blocks between the canister and the shell. The gap between the canister and the rings has 5 mm average and there is one gap of 15 mm between the canister and the discs in one side. Both gaps are air gaps. The other side has the disc in contact with the canister. The package is called Supercontainer and some tens of them are emplaced in the deposition drifts separated

3.6 m. The distance between supercontainers could be higher if there are fractures intersecting the drift. The gap between the supercontainers and blocks between supercontainers, and the host rock has 42.5 mm. The deposition drifts are separated 25 m each other (Figure 1b).

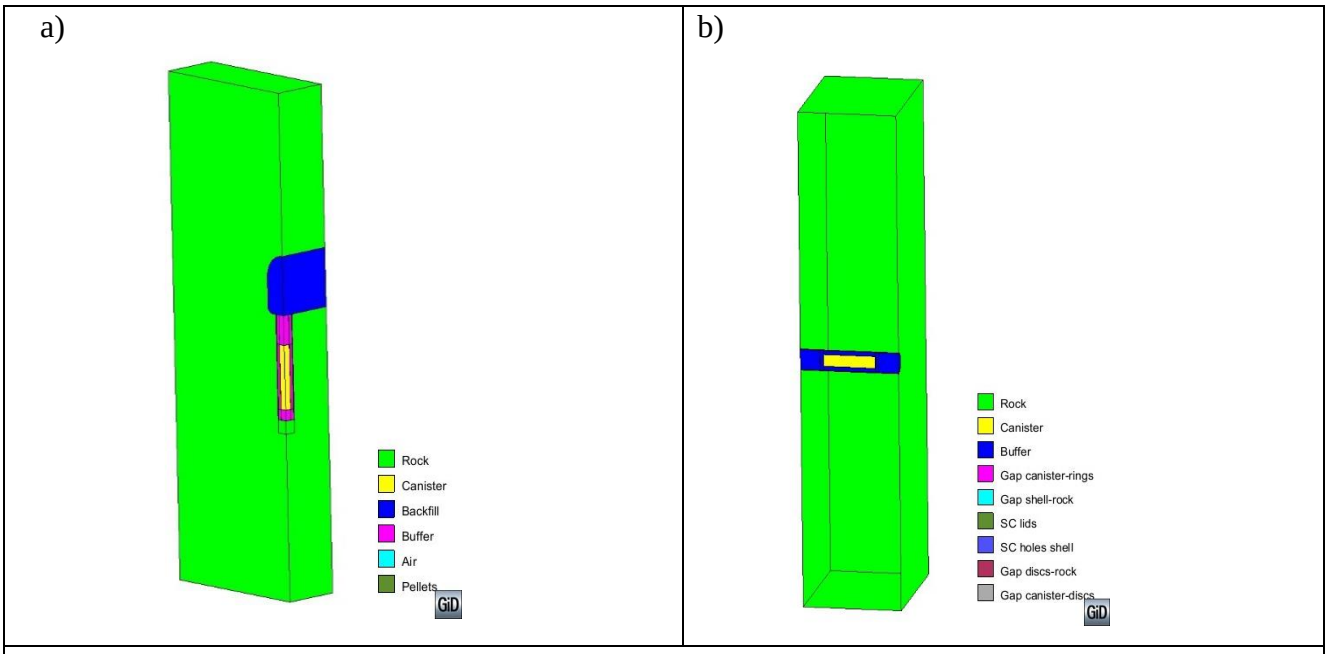

Figure 1: KBS-3V (a) and KBS-3H (b) alternatives in nuclear spent fuel disposal. Box dimensions in KBS-3V are 12.5x4.45x37.7 m and in KBS-3H are 9x12.5x43.7 m

For doing the thermal modelling, all materials were considered as "solid" with a porosity of 0.001. The heat flow at the boundaries was considered zero due to symmetry. The temperatures at the top and bottom surfaces were fixed and calculated by the analytical solution ([3], [4]). The analytical solution considers only a segment heat source and only one material (rock). The analytical solution allows to consider the entire layout taking into account all canisters and the deposition sequence. The influence of the EBS and the dimensions of the canister does not have any influence in the temperature evolution from a few meters from the heat source. The heat inflow from canister followed the power decay of the nuclear spent fuel after 40-50 years cooling with an initial power of 1700 W.

The radiation flow through the air gaps was taken into account ([3], [4], [5]).

3 RESULTS

The analysed cases in KBS-3V and the results are described in Table 1 and in Figure 2. The thermal conductivity of pellets was 0.2 W/(mK) in all cases except the "saturated" case. In this case, the thermal conductivity of pellets was 0.6 W/(mK), the thermal conductivity of water taken as the lowest limit value, and the inner gap was considered closed. The differences between the results obtained with the design method (Ikonen) and the 3-D model increase when the thermal conductivity increases. The temperature calculated in 3-D model is systematically lower than the temperature calculated by Ikonen (except for the unrealistic value of thermal conductivity in blocks of 0.3 W/(mK)).

Table 1. Thermal analysis results in KBS-3V.

Buffer Blocks thermal conductivity (W/(mK))	Ikonen		Calculated		Difference	Difference
	T max (ºC)	Time (years)	T max (ºC)	Time (years)	(T)	(years)
0.3	139.2	6.4	139.48	3.58	-0.28	2.82
0.5	113.1	7.6	112.99	5.6	0.11	2.00
0.75	99.8	10.5	99.31	6.66	0.49	3.84
0.906	97.1	12.2	94.36	6.71	2.74	5.49
1	94.7	13.9	92.09	6.91	2.61	6.99
1.3	75.6		70.52	10.84	5.08	

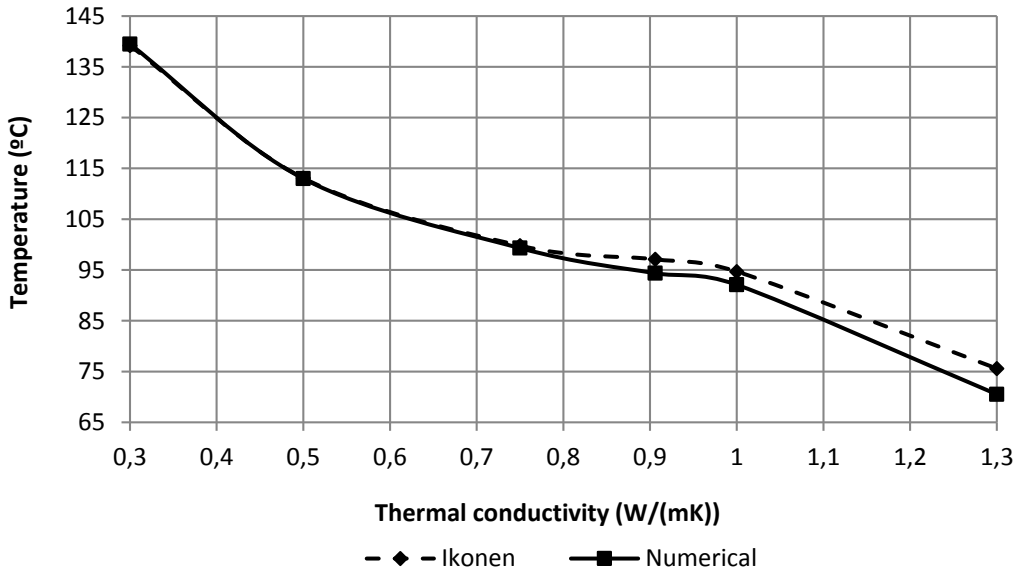

Figure 2. Maximum temperature in canister as function of the thermal conductivity in KBS-3V.

Three cases were run in KBS-3H alternative:

- **Initial condition**: this condition assumes the rock does not supply water and the gap between the buffer and the rock is filled with air. It is an extreme condition. The thermal conductivity of the buffer is 1.0 W/(mK).
- **Artificially wetted outer gap**: In this case, the gap between the buffer and the rock is filled with water. The thermal conductivity of the buffer is 1.0 W/(mK).
- **Saturated**: The buffer is fully saturated and it is assumed that the gaps between canister and buffer rings and between buffer and rock are filled with bentonite. The thermal conductivity of the bentonite is 1.3 W/(mK).

The results are presented in Table 2.

Table 2. Thermal analysis results in KBS-3H.

Reference	T Ikonen [4] (ºC)	t Ikonen [4] (years)	T calculated (ºC)	t calculated (years)
Initial condition	91.7	12.7	90.6	11.8
Artificially wetted outer gap	87.8	14.0	86.6	13.8
Saturated	75.2	18.2	73.9	18.5

The differences in temperature are less than 1.5 ºC and the time for reaching the maximum temperature differences less than one year.

Figure 3 shows how the temperatures calculated in analytical calculation without taking into account the EBS and the thickness of the canister (Ikonen) and the temperatures calculated at the 3-D model converge: at 12.5 m from the axis drift, both temperatures are almost the same.

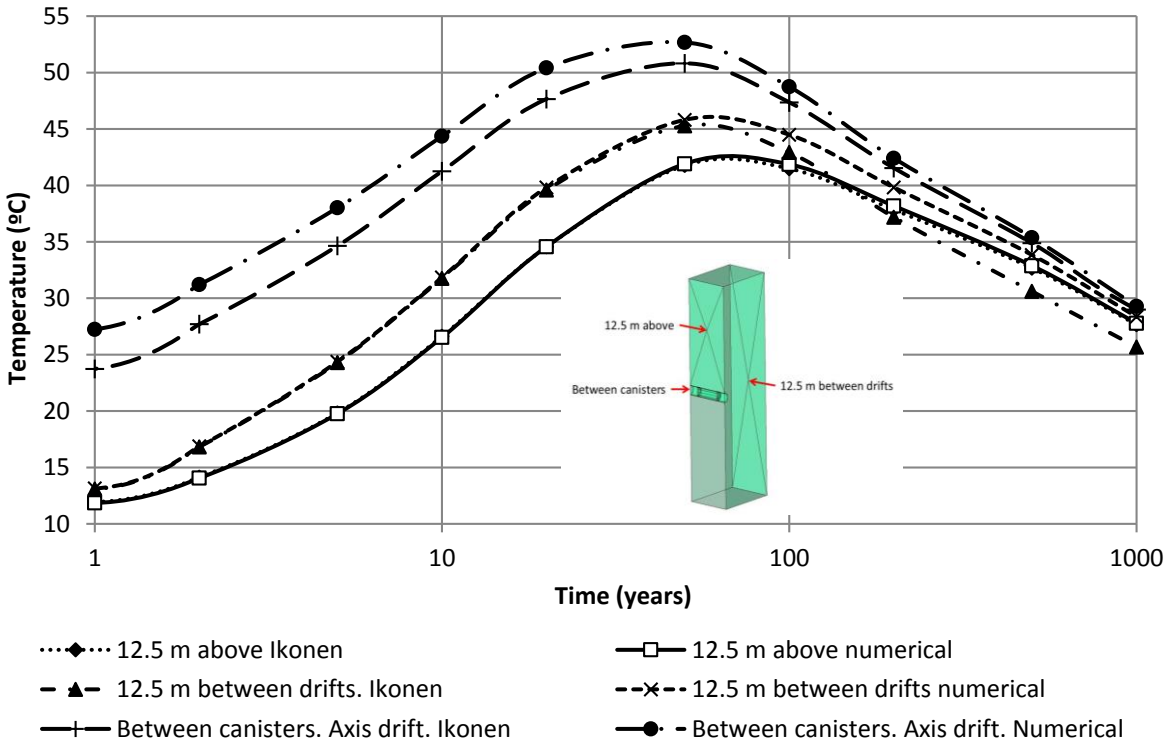

Figure 1. Temperatures evolution in different cases in KBS-3H.

4 CONCLUSIONS

- The thermal design analysis for nuclear spent fuel has been verified with a 3D model and small differences appear in KBS-3V probably due to the lack of axisymmetry of this geometry. KBS-3H design is closer to axisymmetric geometry and the differences are smaller as it can be expected.
- The presence of gaps has influence in the thermal evolution, increasing the temperature in canister.

ACKNOWLEDGEMENTS

This work was financed under a Posiva Oy project. The author agrees to Kari Koskinen and Lasse Koskinen from Posiva and Margit Snellman from SROY Oy their technical and financial support.

REFERENCES

[1] M. Juvankoski, N. Marcos, *Design Basis for Buffer Components*, Posiva Working report 2009-132. Eurajoki, Finland, 2010.

[2] Posiva Oy, *KHS-3H Complementary Studies 2008-2010*, Posiva Report 2013-3, Eurajoki, Finland, 2013.

[3] K. Ikonen, H. Raiko, *Thermal Dimensioning of Olkiluoto Repository for Spent Fuel*, Posiva Working report 2012-56, Eurajoki, finland, 2013.

[4] K. Ikonen, H. Raiko, Thermal analysis of KBS-3H repository, Posiva working report 2015-01, Eurajoki, Finland, 2015.

[5] X. Pintado, J. Autio, *Heat flows in gaps. Radiation and conduction*, 3th Workshop of CODE_BRIGHT users, 2011.

MODELLING OF CONSERVATIVE AND REACTIVE SOLUTE TRANSPORT OF A HIGH-pH INFILTRATION TEST IN CONCRETE

M. Carme Chaparro[a,b,c], Maarten W. Saaltink[a,c], Josep M. Soler[b,c] and Urs K. Mäder[d]

[a] Department of Civil and Environmental Engineering, Universitat Politècnica de Catalunya (UPC), Jordi Girona 1-3, 08034 Barcelona, Spain, e-mail: m.carme.chaparro@upc.edu

[b] Institute of Environmental Assessment and Water Research (IDAEA), CSIC, Jordi Girona 18, 08034 Barcelona, Spain

[c] Associated Unit: Hydrogeology Group (UPC-CSIC)

[d] Rock-Water Interaction, Institute of Geological Sciences, University of Bern, Baltzerstrasse 1-3, CH-3012 Bern, Switzerland

Key words: infiltration test, matrix diffusion, reactive transport, numerical models, concrete.

Abstract. *A laboratory-scale infiltration test was carried out to characterize the transport properties of concrete from the Radioactive Waste Disposal Facility at El Cabril (Spain). A hyperalkaline solution (K-Ca-OH, pH=13.2) was injected into a concrete sample under a high entry pressure in order to perform the experiment within a reasonable time span. The concentrations of the tracers, major elements and pH were measured at the outlet of the concrete sample. First, a conservative transport model was made, which considered diffusion between a mobile zone, with flowing water, and an immobile zone without any advective transport. Porosities and a characteristic time for matrix diffusion were obtained by fitting the experimental data to the model results. Then, a reactive transport model was built. The cement paste consists of C-S-H gel, portlandite, ettringite, calcite and gypsum, together with residual alite and belite. Overall the results show dissolution of alite, belite, gypsum and quartz and precipitation of C-S-H gel, portlandite, ettringite and calcite.*

1 INTRODUCTION

Concrete is a porous material that consists of cement paste and coarse and fine aggregates. The cement paste is composed of the hydration products of the cement, mainly C-S-H (calcium silicate hydrate), portlandite, ettringite and/or monosulphate together with smaller amounts of other hydration products. The way these phases are arranged geometrically can be quite complex.

When concrete is exposed to evaporation, the pressure gradient may become high and flow of water, and hence, advection and dispersion can become important. This is the case of the radioactive waste facility at El Cabril [(i)]. In this work, we study solute transport in concrete taking into account diffusion, dispersion and advection. We treat the heterogeneity of concrete by means of matrix diffusion [(i,ii)]. The goal of this work is to improve the understanding of

processes, transport properties and reactivity of concrete. In particular, we studied the concrete from the radioactive waste disposal facility at El Cabril.

2 INFILTRATION TEST

The test consisted of injecting a high-pH solution (pH=13.4) with tracers (lithium, bromide and deuterium) into a sample using a pulse injection. Afterwards, the same solution, but without tracers, was injected until the end of the test. A device that allows injecting the solution with a high infiltration pressure was used. The infiltration solutions were composed of distilled water with 10.6 g/l of KOH and 0.1 g/l of $Ca(OH)_2$ giving a pH of 13.4. The outlet solution was collected by syringes. The measured components were Ca, SO_4, K, Na and pH. Data obtained are compared with the ones calculated by the numerical model. During the experiment, the hydraulic conductivity decreased with time by a factor of 1000, which could be due to mineral precipitation.

3 NUMERICAL MODEL

Simulations of the laboratory test were performed in order to interpret the experiment and deduce transport processes and chemical reactions. The numerical models consider conservative and reactive transport.

The conceptual model is based on matrix diffusion, which is a transport mechanism that allows solute transfer between a mobile zone and an immobile zone. The mobile zone represents the well-connected pores with solute transport by advection, dispersion and diffusion. The immobile zone represents the matrix, where solutes are transported only by diffusion. We compared three geometries of the porous medium so as to represent the immobile zone: slabs, spheres and tubes. The models were calibrated by fitting the porosity of the mobile zone and the characteristic time for diffusion in the immobile zone to the breakthrough curves of deuterium and bromide (lithium was not used due to lack of data).

To simulate reactive transport, slabs were considered as the geometry of the immobile zone. The calibrated parameters obtained in the conservative transport model were used. Minerals are only considered in the immobile zone. The cement paste consists of alite, belite, gypsum, calcite, C-S-H gel, portlandite and ettringite. The aggregates are composed of quartz. The initial pore water of the immobile zone is in equilibrium with the cement phases, and the water in the mobile zone is in accordance with the measured data (early breakthrough). Two numerical models were compared, one using a high surface area (equilibrium) and the other with a low surface area of portlandite.

The mesh is composed of 561 nodes and 560 linear elements. The *y* axis represents the mobile zone with a length of 5.52 cm, and contains 50 nodes. For each node in the mobile zone, there is an immobile zone (*x* direction) with 10 nodes.

The simulations were carried out using the codes Code_Bright[(iii)] and Retraso-Code_Bright[(iv)].

4 RESULTS AND DISCUSSION

Figure 1 shows the model results for the deuterium. A double-porosity model is compared with a single porosity model and with the experimental data. A single-porosity model without matrix diffusion cannot reproduce the experimental data. However, excellent agreement between the double-porosity model and experimental data for deuterium has been obtained. Bromide behavior cannot be reproduced using a conservative transport model. Even when a retardation coefficient is applied, the results are not satisfactory (not shown). From the calibration of deuterium, similar porosities are obtained for all geometries. We found porosities of the immobile zone much higher than that of the mobile zone (about 0.14 and 0.028, respectively). However, the characteristic time depends on the geometry considered; the values obtained are between 40.7 and 316 days. For conservative tracers, such as deuterium, the fits for the three geometries were practically identical. This means that this type of tracer test cannot be used to determine the geometry of the immobile zone.

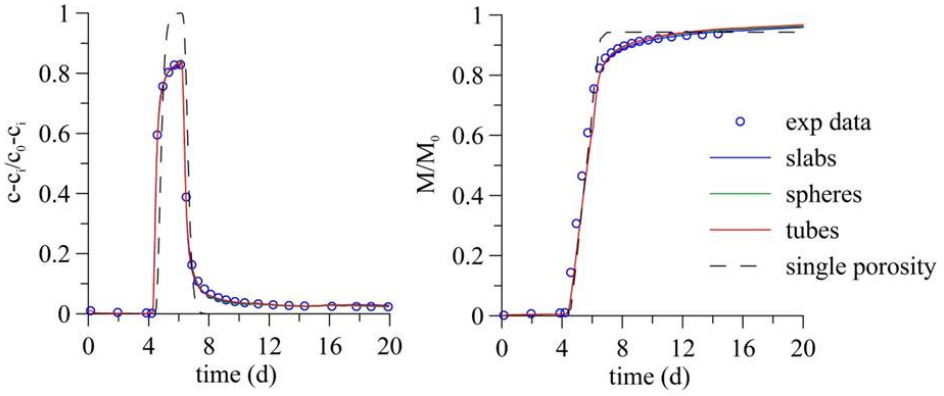

Figure 1: Evolution of relative concentration and cumulative mass for deuterium. Double-porosity model results (continuous lines) are compared with the experimental data (points) and with a single-porosity model (dashed lines)

The reactive transport model compares two different models, one with portlandite in equilibrium (high initial surface area) and another one with portlandite reaction controlled by kinetics (low initial surface area). When porlandite is in equilibrium, modelled Ca concentrations are practically constant and cannot reproduce the measured data, where the solution is first undersaturated with respect to portlandite and later oversaturated. The model with porlandite controlled by kinetics can reproduce this behaviour. The other components are similar for both models obtaining a good fit to the measured data. The calculated changes in mineralogy show dissolution of alite, belite, gypsum and quartz. Near the mobile zone ettringite dissolves and calcite precipitates. Both models show similar results for C-S-H gel; it first dissolves near the mobile zone and then precipitates due to clinker dissolution. When the initial surface area is higher, there is higher precipitation of portlandite and calcite, which keeps the Ca concentration constant. But the measured data suggest slower precipitation of portlandite (low surface area). The numerical model assumed that all reactions took place in

the immobile zone. However, permeability could have decreased due to mineral precipitation (calcite, portlandite and C-S-H gel) moving in reality across the interface into the mobile zone In the immobile zone, both models show an increase in porosity because of mineral dissolution (clinker phases, ettringite and gypsum).

5 CONCLUSIONS

Conservative and reactive transport models were developed in order to study transport processes and chemical reactions in a laboratory infiltration test using concrete. Our numerical models demonstrated that a double-porosity conceptual model should be considered for conservative and reactive transport of solutes in concrete.

From the numerical model for deuterium similar porosities are obtained for all the considered geometries. However, characteristic time depends on the geometry. The three geometries show similar fits, indicating that this kind of test cannot be used to determine the geometry of the immobile zone. The bromide behaviour cannot be reproduced even when a retardation coefficient is applied.

Reactive transport models show that when portlandite is at equilibrium the model cannot reproduce outlet Ca concentration, but the model with portlandite controlled by kinetics can. Changes in mineralogy show dissolution of alite, belite, gypsum, quartz and ettringite, and precipitation of portlandite, C-S-H gel and calcite. The permeability could have decreased due to precipitation of portlandite, C-S-H and/or calcite.

Acknowledgement. This work was funded by a Research Grant from the Technical University of Catalonia (UPC), the Spanish Ministry of Economy and Competitivity trhough the project HEART (CGL2010-18450) and ENRESA (Spanish Nuclear Waste Management Company).

6 REFERENCES

[i] Chaparro, M. C. (2016), Transport of Water, Vapour, Heat and Solutes in Concrete for Storing Radioactive Waste, UPC, Department of Geotechnical Engineering and Geosciences. PhD Thesis.

[ii] Chaparro, M. C., Saaltink M. W., Soler J. M., Slooten L. J., Mäder U. K. (2015), Modelling of matrix diffusion in a tracer test in concrete. Transport in Porous Media, 111:27-40, doi: 10.1007/s11242-015-0579-5.

[iii] Olivella, S., A. Gens, J. Carrera, E.E. Alonso (1996), Numerical formulation for a simulator (CODE_BRIGHT) for the coupled analysis of saline media, Eng. Comput.,13(7), 87-112.

[iv] Saaltink, M. W., F. Batlle, C. Ayora, J. Carrera, S. Olivella (2004), RETRASO, a code for modelling reactive transport in saturated and unsaturated porous media. Geologica Acta. 2, 235-251.

HYDRO-MECHANICAL MODELLING OF GAS INJECTION EXPERIMENTS IN BOOM CLAY

Laura Gonzalez-Blanco[*], Enrique Romero[*] and Cristina Jommi[†]

[*] Division of Geotechnical Engineering and Geosciences
Department of Civil and Environmental Engineering
Technical University of Catalonia (UPC)
Campus Nord UPC, 08034 Barcelona, Spain
e-mail: laura.gonzalez.blanco@upc.edu ; enrique.romero-morales@upc.edu

[†] Department of Geoscience and Engineering
Faculty of Civil Engineering and Geosciences
Delft University of Technology
Stevinweg 1, 2628 CN Delft, The Netherlands,
e-mail: c.jommi@tudelft.nl

Key words: Waste disposal, gas transport, preferential air flow.

Abstract. *Gas migration through a potential host clay formation for the geological disposal of radioactive waste was experimentally studied. In this paper, results of finite element numerical simulations performed with the CODE_BRIGHT are compared with relevant experimental measurements. An embedded fracture permeability model has been used to explain the gas breakthrough observations. This model allows tracking the degradation of the soil sample under gas pressurization (increasing gas permeability) and helps in the comprehension of the local coupled processes dominating the response of the material.*

1 INTRODUCTION

The long-term behavior of clay barriers for the geological disposal of radioactive waste is currently receiving more attention. A significant issue in the long-term performance of clay buffers and the surrounding host rock concerns the generation and migration of gases. Actually, in the post-closure phase of a disposal system, gases can be produced as a result of the anaerobic corrosion of metal canisters, radiolysis, microbial degradation of organic waste and radioactive decay [i]. The pressure will increase as a result of gas generation in an almost impermeable geological medium in the near-field of a repository. Under high gas pressures, the mechanical and hydraulic properties of the host rock and the barrier system are expected to change significantly, which eventually may lead to the release of the produced gases.

To improve the knowledge on Boom Clay response to gas migration and the predictive capabilities on the long-term behavior as host formation, a comprehensive series of air injection tests under oedometer conditions was performed [ii]. Relatively fast volume rate air injection tests (air pulse tests) were carried out to give priority to dominant single-phase air flow mechanisms associated with the opening of stress dependent discontinuities. The tests were specifically designed on samples with oriented bedding planes to investigate the coupled hydro-mechanical mechanisms during gas injection and dissipation. Volume changes were allowed in the experimental setup, and the deformation response was analyzed during air injection at two different rates (2 and 100 mL/min).

Particular attention was given to the change in the pore network in order to detect the opening of fissures or discontinuities due to the air migration, by analyzing the pore size

distribution (PSD) data from mercury intrusion porosimetry (MIP) before and after the gas injection tests. The PSD data was used to show the evidence of preferential pathways formed during gas injection and dissipation and to calibrate the hydraulic laws used in the numerical simulations of the tests.

2 MODEL DESCRIPTION

A 2D axisymmetric representation of the sample was selected. Both for the constitutive model and the geometry of the problem, simple approximations were made, still being able to capture the consequences of preferential path development (Figure 1). The sample was modelled by two zones with different hydraulic properties: the matrix and the zone of fracture development (ZFD) in which the dominant advective flow of gas occurs. In the choice of the latter, a single predefined central zone was chosen, renouncing to investigate the local distribution of the fractures, but still keeping the possibility of reproducing the global effect of the localized preferential paths on the sample response. For the matrix and the ZFD the same mechanical parameters were chosen, but different hydraulic models were used. To properly simulate the test, it was necessary to include both the injection and recovery systems in the model, which corresponded to the drainage lines of the experimental set-up. If these had not explicitly included in the numerical model, the actual injection and outflow pressures history at the boundaries of the sample would not have been properly assigned, disregarding the change in the density of the pressurized mass of air.

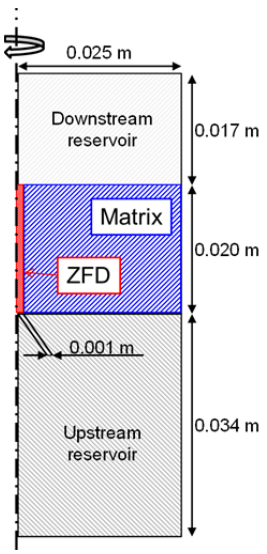

Figure 1. Geometry and materials used in the simulations.

The adopted mechanical model was the elastoplastic model BBM (Barcelona Basic Model, [iii]). In order to simulate the effects of the localized fissures along the bedding planes (gas pathways parallel to bedding planes), the embedded fracture permeability model [iv] was applied in the ZFD. This hydraulic model can take into account the variation of the intrinsic permeability (k), and the capillary air entry pressure (P) with fracture aperture (b), which depends on strain (ε).

$$k = k_0 + \frac{b^3}{12s} \tag{1}$$

$$P = P_0 \sqrt[3]{k_0/k}$$

$$b = b_0 + \Delta b = b_0 + s\Delta\varepsilon = b_0 + s(\varepsilon - \varepsilon_0)$$

where k_0 and P_0 are the reference intrinsic permeability and capillary pressure which eventually can correspond to the matrix; s is a characteristic dimension, b_0 the initial aperture and ε_0 a threshold strain.

2.1. Model parameters

Mechanical parameters required for the BBM model in the present calculations were determined from different hydro-mechanical tests performed during the experimental study.

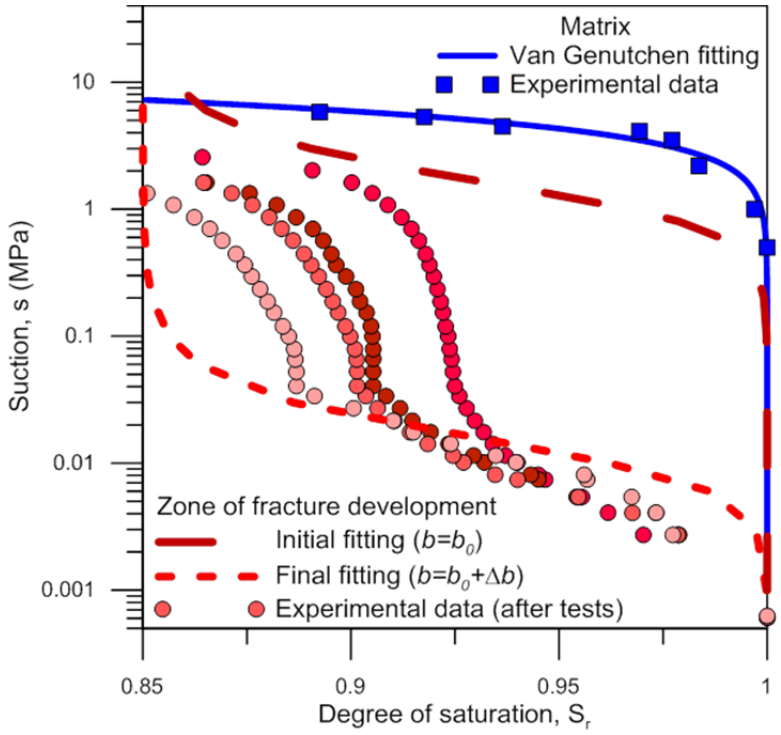

Figure 2. Experimental water retention curves before (matrix) and after (fracture) air injection tests together with their modelling curves.

The parameters for the embedded fracture permeability model were obtained by fitting by using experimental data. An initial aperture of 100 nm, equivalent to the dominant pore mode of the matrix, was selected. The threshold strain, ε_0, and the characteristic dimension, s, were fitted so as to achieve a final capillary pressure in the ZFD similar to the one determined by MIP after the air injection tests (Figure 2).

2.2. Boundary conditions

To simulate oedometer conditions, null vertical displacements at the bottom of the system and null radial displacement on the sample lateral wall were imposed.

Before starting air injection, the sample was fully saturated, as well as both reservoirs. At the beginning of the injection the upstream reservoir was full of air at a pressure of 0.5 MPa. An injection pressure ramp was then applied at the bottom of the injection reservoir, which followed the recorded data during the test. The dissipation stage started once the injection pressure reached the maximum pressure of 4 MPa. Afterwards, the bottom boundary became impermeable along this dissipation stage forcing the accumulated air in the reservoir to flow upwards.

The pressure of the downstream pressure/volume controller was kept constant at 0.5 MPa during the tests. This device is capable of maintaining the pressure by changing the volume as the air flows through the sample. However, when the tank of the controller is full, it is not able to keep the pressure anymore if the air flow continues and thus the pressure begins to rise. In contrast, the upper reservoir in the simulation has a fixed volume. As a result, an increase in the outflow pressure must be imposed in the simulation to properly model the boundary conditions. Accordingly, the pressure boundary condition in the downstream reservoir was set constant in the first stage of the simulation - water pressure at 0.5 MPa - and was increased up to 1.5 MPa in the last stage.

3 RESULTS

The results of the computed injection and outflow pressure response as a function of time together with the outflow volume and the axial strain are shown in Figure 3 in comparison with experimental results for the sample tested at slower injection rate (2 mL/min). The air pressure in the bottom of the sample during the dissipation stage is acceptably well fitted. Good agreement is found on the fluid pressure at the top, computed as the maximum between air and water pressure. Moreover, the time in which the outflow takes place compares well with the measured one. The outflow volume, computed as the sum of water and air volumes, fits well with the experimental measurements. The computed sample volume change represented by the average axial strain is also reasonably well reproduced. The sample at slow air injection rate undergoes an expansion during the injection -effective stress decrease- followed by a compression while the constitutive stress increases. The computed results show the same expansion, while a slightly larger compression than the measured experimental values is predicted.

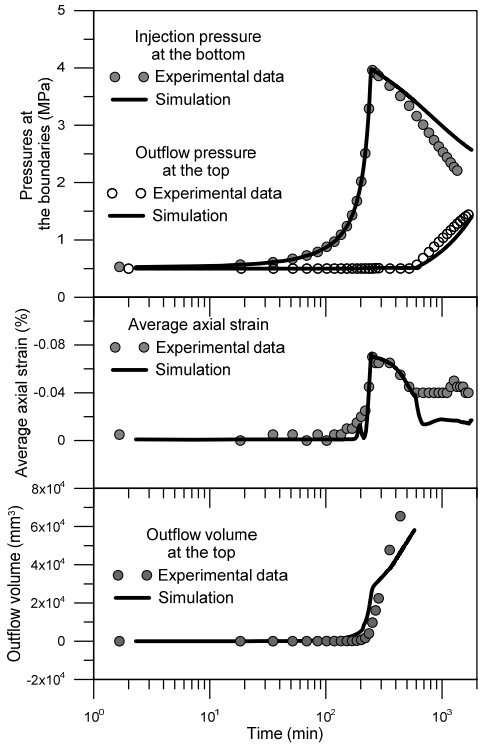

Figure 2. Computed versus measured in the ZFD: a) injection and recovery pressures (top); b) average axial strains (middle); c) outflow volume (bottom). Slower injection test.

The internal sample response is depicted in Figure 4, with contour plots to better understand the influence of the embedded fracture response. It is worth noting that the opening of the fracture plays an important role in terms of air dissipation. On the one hand, only when the air pressure increased enough, the fracture opens and becomes desaturated, allowing the air to flow. On the other hand, as the air pressure decreases due to the outflow, the fracture gradually closes up over the time. The matrix of the clay presents a significant delayed behavior, as its permeability does not change as the same rate. Moreover, it remains fully saturated after the air passage.

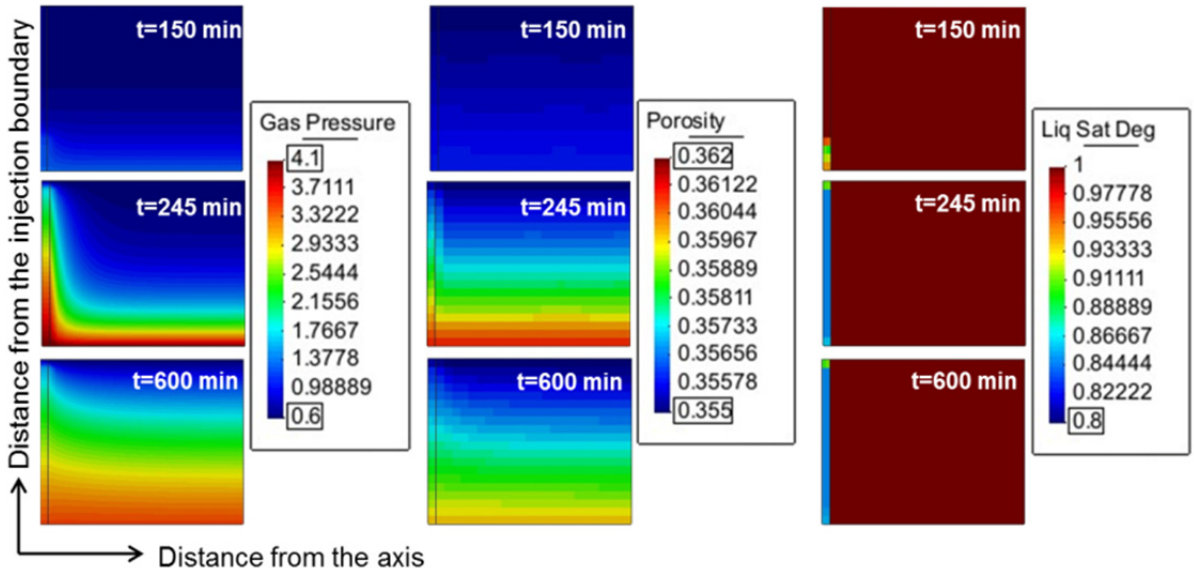

Figure 4. Simulated distribution of absolute gas pressure (left, in MPa), porosity (middle) and liquid degree of saturation (right) during the air injection (t=150 min), at shut-off (t=245 min) and the dissipation (t=600 min).

The parameters of the embedded fracture model were calibrated by comparison with the slow injection test. To demonstrate the predictive capability of the numerical model, the fast air injection (100 mL/min) test was simulated with the previous set of parameters, representing a blind test (Figure 5). The pressure release in the simulation is slower than the measured, and thus the average axial strain is slightly higher. However, the overall deformation behavior is well captured.

4. CONCLUSIONS

The comparison between the experimental data and the model predictions shows encouraging agreement. The simple numerical model implemented for the analysis of these oedometer tests provides some interesting information on the local hydro-mechanical coupled response of Boom Clay subjected to gas pressurization and transport. However, realistic modelling in a more general geometric configuration can be achieved only by integrating the embedded fracture model in all the elements. Including random permeability (or porosity) fields would allow heterogeneity to automatically develop fracture patterns, without the need for a pre-defined fracture zone. The experimental and numerical studies continue with the analysis of the influence of the inherent anisotropic structure of the Boom Clay.

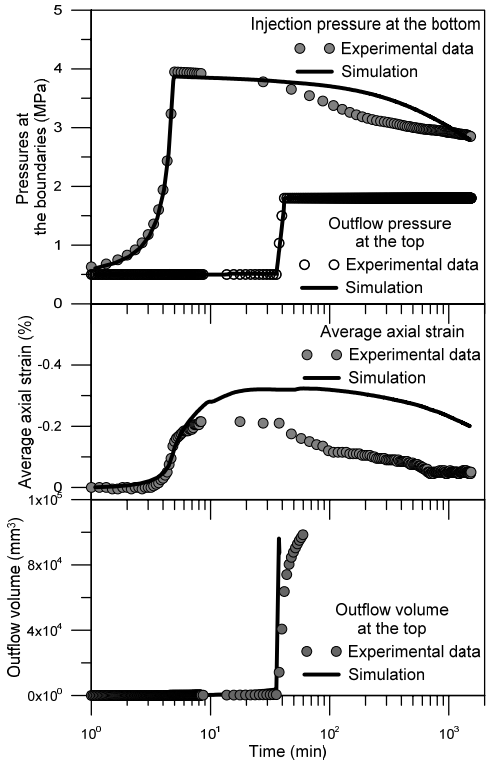

Figure 5. Computed versus measured in the ZFD: a) injection and recovery pressures (top); b) average axial strains (middle); c) outflow volume (bottom). Faster injection test.

ACKNOWNLEDGE

Financial support of ONRAF/NIRAS (Belgium) is greatly acknowledged.

REFERENCES

[i] ONDRAF/NIRAS, "Research, Development and Demonstration (RD&D) Plan for the geological disposal of high-level and/or long-lived radioactive waste including irradiated fuel of considered as waste, State-of-the-art report as of December 2012," ONDRAF/NIRAS, report NIROND-TR 2013-12 E, 2013.

[ii] Gonzalez-Blanco, L, E. Romero, C. Jommi, X. Li, X. Sillen, (in press), 'Gas migration in a Cenozoic clay: experimental results and modelling' Geomechanics for Energy and the Environment (doi: 10.1016/j.gete.2016.04.002)

[iii] Alonso, E. E., A. Gens, A. Josa, 1990, 'A constitutive model for partially saturated soils' Géotechnique, Vol. 40, No. 3, pp. 405–430.

[iv] Olivella, S., E. E. Alonso, 2008, 'Gas flow through clay barriers' Géotechnique, Vol. 58, No. 3, pp. 157–176.

EFFECT OF OPEN-GAPS BETWEEN NUCLEAR SPENT FUEL DISPOSAL CONTAINER AND HOSTING ROCK

I.P. Damians[*], S. Olivella[*], and X. Pintado[†]

[*] Department of Geotechnical Engineering and Geosciences
Universitat Politècnica de Catalunya – BarcelonaTech (UPC)
Campus Nord UPC, 08034 Barcelona, Spain
Email: ivan.puig@upc.edu

[†] B+TECH Oy; Laulukuja 4 00420 Helsinki, Finland
Email: xavier.pintado@btech.fi

Key words: TH 3D model, Gap, Onkalo

Abstract. *The KBS-3H alternative is composed by horizontally placed supercontainers comprising the canisters with the nuclear spent fuel surrounded by compacted bentonite blocks (buffer) enclosed in a perforated metal shell. The gaps between the supercontainers and blocks and the host rock have direct effects on the buffer behaviour. This paper presents a Thermo-Hydraulic 3D numerical model generated in order to analyse a particular geometry assuming two different gap state conditions and providing results of the degree of saturation evolution.*

1 INTRODUCTION

Nuclear spent fuel management is done in a way that is not harmful to organic nature. Posiva Oy is an expert organization responsible for the final disposal of nuclear spent fuel in Finland and it is constructing the final disposal in Onkalo [1]. The current paper presents some results from a TH 3D numerical model generated in order to analyze the temperature and degree of saturation evolution of a nuclear spent fuel disposal with a sequential emplacement of canisters in a drift, assuming two different gap state conditions between the buffer blocks and the supercontainer shell and the host rock in KBS-3H design alternative [2].

2 MODEL GEOMETRY AND MATERIAL PROPERTIES

The drift was assumed to be placed at 425 m-depth. The model was built assuming 100 m vertical separation of host rock above and below the drift (i.e., distance to boundaries; which was determined to be far enough in order to assure the proper temperature dissipation [3]). After 1 year with empty tunnel and atmospheric pressure imposed at internal drift surfaces, eight canisters (and related components) were assumed to be serially distributed and horizontally arranged (with 2º tilt longitudinally), and the separation between parallel tunnels was fixed to be 25 m (see Figure 1a). The total length of the tunnel is about 107 m, and supercontainers separation is variable due to rock fractures presence (e.g., from 3.5 m up to 16 m distance for the longest case). Description about how to deal with intersecting fractures is described in [2]. Bentonite buffer blocks separate both containers and the host rock and containers themselves (see Figure 1b-c). A gap of 45 mm-thick was assumed between the buffer blocks and the host rock, which performs the actual “gap” at Installation state,

otherwise "slot" due to buffer block swelling at Initial state (see Figure 1d and Figure 2). To perform this buffer block swelling effect and gap closure at Initial state, a certain thickness of block is defined as "interface" material, which shares properties with closed gap (now called "slot") with equivalent properties from block swelling). Calculations at this "Initial state" assume that the bentonite has flowed out from the supercontainer and the material which fills the gap (slot) can be considered as a solid. Part of the material inside the supercontainer (interface) has the same properties the material at the slot and the rest of the blocks remain unchanged. This is a simplification because the gap filling process cannot be simulated. Table 1 presents the material properties at initial conditions for both Installation and Initial states. Table 2 presents the buffer blocks drift components for these states.

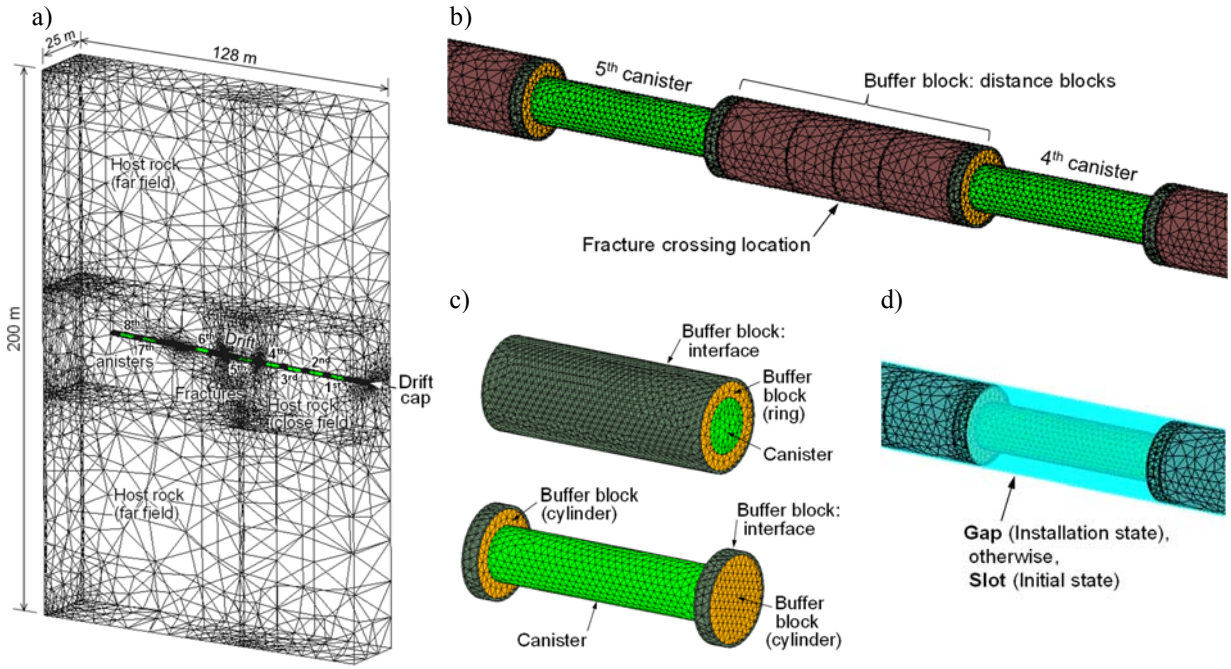

Figure 1: Entire drift 3D model mesh and main geometry dimensions (a), canister-to-canister mesh detail (b), super-container components (c), and gap/slot detail (d).

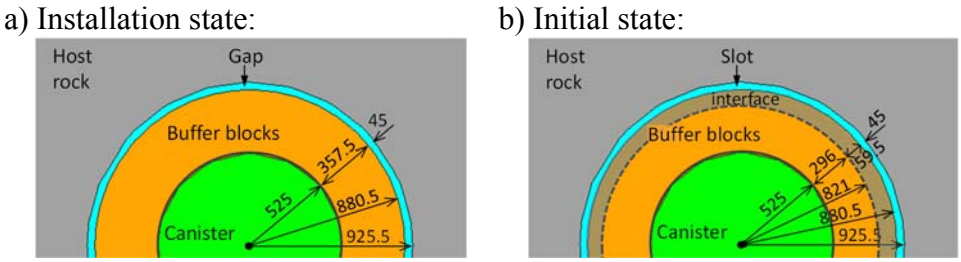

Figure 2: Super container cross-section geometry: Installation (a), and Initial (b) states

3 RESULTS

Figure 3 presents the canisters temperature evolution from canisters emplacement for Installation state with actual gap presence, and Initial state with closed gap and interface/slot equivalent properties) states. As it can be observed, slightly higher maximum temperature is

reached at Installation state: about 70ºC at 3rd canister after 4 years whereas in Initial state was about 67ºC after 15 years from canisters emplacement. Figure 4 shows the evolution of the degree of saturation at several points around 5th canister. Despite the trends and minimum degree of saturation are approximately the same at points 4 and 5, slowed saturation process was done in points 1, 2 and 3. The point 1 presented the most dramatic trending change, where, at Initial state, the saturation was reached 4 years faster than at Installation state.

		Materials:					
Parameters		Host rock	Fractures	Buffer blocks	Gap / Slot	Canister	Units
Porosity		0.005	0.005	(Table 2)	(Table 2)	0.01	-
Intrinsic permeability		1.52e-19 at close field, 1.52e-17 at far field [(a)]	1e-15	k_0 = 5.59e-21 [(b)]	Initial state: k_0 = 5.59e-21 [(b)] Installation: 1e-16 (fixed)	1e-24	m^2
Water retention curve [(c)]	P_0	1.5	1.5	31.25	0.05	31.25	MPa
	λ	0.3	0.3	0.5	0.3	0.5	-
Relative permeability [(d)]		3	3	3	3	3	n-power
Dry thermal conductivity		2.82	2.82	0.22	Initial: 0.22 Install.: 0.02	390	W/mK
Saturated thermal conductivity		2.82	2.82	1.25	Initial: 1.25 Install.: 0.6	390	W/mK
Solid unit weight		2743	-	2780	Initial: 2780 Installation: 0	8930	kg/m^3
Solid phase specific heat		746	-	830	1000	390	J/kgK
Initial liquid pressure		hydrost.[(e)]	hydrost.[(e)]	(Table 2)	(Table 2)	-20	MPa
Initial Temperature		10.5	10.5	10.5	10.5	50	ºC

Notes: [(a)] Higher value of permeability at far-field rock material (i.e., from 20 m up to 100 m above and below the tunnel) to take into account the network fracture capacity to keep the pressure almost constant at 20 m from the axis drift; [(b)] Intrinsic permeability defined as per the following exponential law: $k_{ii} = k_0 \exp\{b(\phi - \phi_0)\}$, which returns k_0 =5.59e-21 (for b =15 and ϕ_0 =0.438); [(c)] Water retention curve according to Van Genuchten model (λ: shape function); [(d)] Relative permeability $k_{rl} = (S_r)^n$, where S_r: degree of saturation; [(e)] Hydrostatic-linear law from 3.25 MPa (top) to 5.25 MPa (bottom boundary).

Table 1: Material properties starting conditions

	Buffer block materials:									
	Buffer block: Cylinder			Buffer block: Ring			Distance block			
Installation:	block	interface	gap	block	interface	gap	block	interface	gap	Units
ϕ	0.369		0.99	0.322		0.99	0.384		0.99	-
S_r	0.807		1	0.644		1	0.936		1	-
P_l	-23		0.1	-37		0.1	-11.7		0.1	MPa
Initial:	block	interface	slot	block	interface	slot	block	interface	slot	
ϕ	0.369	0.689		0.322	0.689		0.384	0.664		-
S_r	0.807	0.861		0.644	0.805		0.936	0.961		-
P_l	-23	-18.5	0.1	-37	-23	0.1	-11.7	-9	0.1	MPa

Table 2: Installation and Initial states starting porosity (ϕ), degree of saturation (S_r), and liquid pressure (P_l) for buffer block drift components

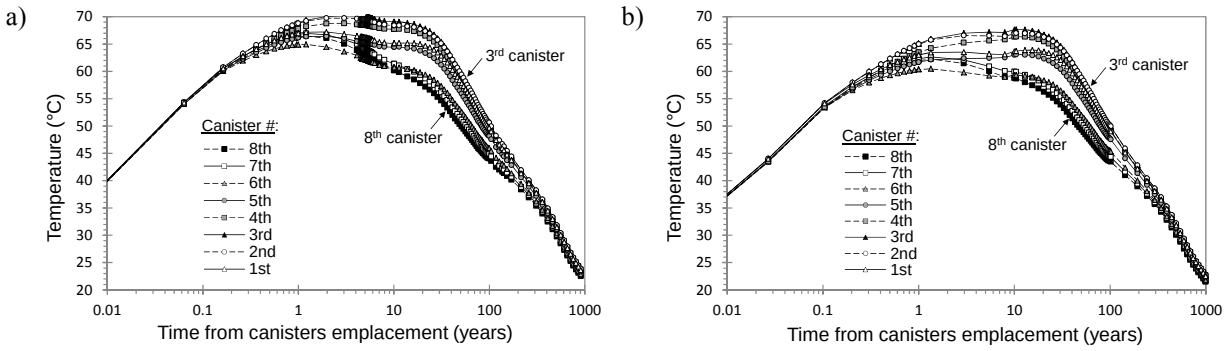

Figure 3: Temperature evolution at canisters center: Installation (a) and Initial (b) states.

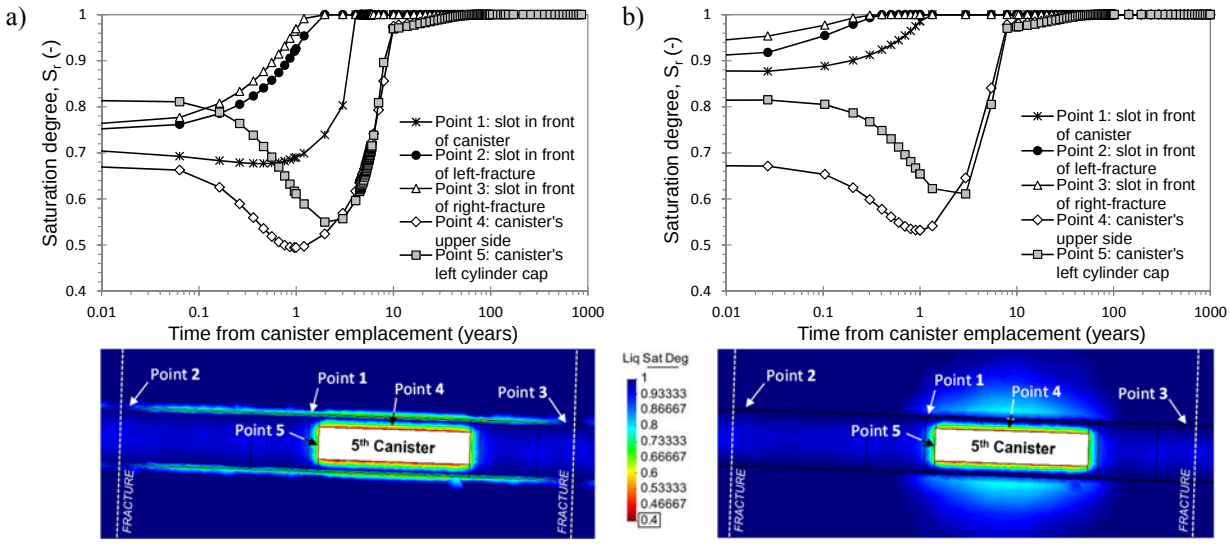

Figure 4: Degree of saturation evolution at several points around 5th canister: Installation (a), and Initial (b) states. Figure results after 1 year from canister emplacement.

4 CONCLUSIONS

- The numerical TH 3D model for studying nuclear spent fuel disposal looks promising for further sensitivity analyses.
- In the current study, the presence of actual gap condition between the buffer blocks and the host rock resulted in direct effect on KBS-3H design alternative behaviour.

ACKNOWLEDGEMENTS

This work was financed by B+Tech Oy (Finland) under a POSIVA Oy project.

REFERENCES

[1] Posiva Oy, 2009. Olkiluoto Site Description 2008, Posiva Report 2009-01, Eurajoki, FI.

[2] Posiva Oy, 2013. KHS-3H Complementary Studies 2008-2010, Posiva Report 2013-3, Eurajoki, Findland.

[3] E. Toprak, N. Mokni, S. Olivella, and X. Pintado, 2013. Thermo-Hydro-Mechanical Modelling of Buffer, Synthesis Report, Posiva Report 2012-47, Eurajoki, Findland.

OVERVIEW OF THE MODELING OF GEOLOGIC CARBON STORAGE USING CODE_BRIGHT

Víctor Vilarrasa*

*École Polytechnique Fédérale de Lausanne, EPFL, Switzerland
e-mail: victor.vilarrasariano@epfl.ch

Keywords: CO_2 storage, Overpressure evolution, Cold CO_2, Thermo-hydro-mechanical couplings, Induced seismicity, CO_2 leakage, Caprock integrity

Abstract. *The huge amounts of carbon dioxide (CO_2) that we are emitting to the atmosphere should be reduced to mitigate climate change. According to the International Energy Agency, geologic carbon storage has the potential to contribute to reduce around 20 % of the CO_2 emissions, which would represent injecting around 8 Gt/yr by 2050 in deep geological formations. Such injection mass rate will induce large overpressures, reducing the effective stresses. Furthermore, CO_2 will generally reach the storage formation at a lower temperature than that corresponding to the geothermal gradient, which will induce thermal stress reduction. The effective stress reduction induced by both overpressure and cooling will cause rock deformation and potential caprock and fault stability issues, which could induce seismicity and damage the caprock sealing capacity that prevents CO_2 leakage. Our modeling activities of geologic carbon storage using CODE_BRIGHT have focused on understanding how cold CO_2 injection affects rock stability in order to define geomechanically safe injection conditions. We have shown that a proper site characterization and pressure management can allow storing CO_2 in deep geological formations safely, without inducing felt induced seismicity and with no CO_2 leakage.*

1. INTRODUCTION

The current carbon dioxide (CO_2) emissions, in the order of 35 Gt/yr, are causing anthropogenic climate change. To mitigate this climate change, governments have recently reached an agreement at the COP21 meeting in Paris to take the necessary measures to avoid a temperature increase higher than 2 °C with respect to the pre-industrial temperature. According to the International Energy Agency (IEA), such objective can be achieved by reducing CO_2 emissions by more than half with respect to the current CO_2 emissions by 2050[i]. Geologic carbon storage has the potential to contribute to reduce around 20 % of the future CO_2 emissions[i], which would represent injecting around 8 Gt/yr by 2050 in deep geological formations.

Geologic carbon storage consists in injecting and keeping CO_2 in deep geological formations, such as depleted oil and gas fields, unminable coal seams and deep saline aquifers[ii]. Sedimentary formations are very suitable to store CO_2 because high-permeable formations (potential storage formations) alternate with low-permeable formation (potential caprocks). The high-permeable formations allow injecting CO_2 without inducing large overpressures and the low-permeable formations prevent the buoyant CO_2 from migrating upwards[iii]. Suitable storage formations are located at depths deeper than 800 m because at these depths the pressure (P) and temperature (T) conditions ensure that CO_2 will remain in supercritical conditions, i.e., P>7.382 MPa and T>31.04 °C[iv]. Supercritical CO_2 has a liquid-like density, converting the storage efficient in terms of volume, and a gas-like viscosity, which facilitates CO_2 flow within the storage formation. CO_2 density at the storage conditions is lower than that of the resident brine, so CO_2 tends to float due to buoyancy. Thus, maintaining the caprock sealing capacity is crucial to prevent CO_2 leakage.

CO_2 will, in general, reach the storage formation at a lower temperature than that of the rock, especially at high flow rates[v]. Furthermore, injecting CO_2 in dense (cold) state is energetically efficient because the compression costs at the wellhead are significantly reduced[vi]. Therefore, thermo-mechanical effects caused by cold CO_2 injection will be common. Cold CO_2 injection generates a cold region around the injection well, inducing an effective stress reduction that, in addition to that induced by overpressure, may compromise rock stability[vii] and induce microseismicity[viii]. To achieve a safe CO_2 storage, without CO_2 leakage and without felt induced seismic events, the coupled thermo-hydro-mechanical processes caused by cold CO_2 injection in deep saline formations should be understood. This understanding should lead to the definition of the maximum sustainable injection pressure and the maximum temperature drop that can be undergone safely.

Here, we summarize the main key findings of the modeling activities that have allowed us to conclude that a proper site characterization and pressure management can allow storing CO_2 in deep geological formations safely, without inducing felt induced seismicity and with no CO_2 leakage.

2. EQUATION OF STATE FOR CO_2

To simulate non-isothermal CO_2 injection into CODE_BRIGHT[ix,x], some subroutines were extended by implementing specific thermodynamic functions and fluid properties relationships. The extension of CODE_BRIGHT to simulate CO_2 injection is included in the manual and is available in the latest version of the code.

CO_2 density is calculated through the Redlich and Kwong[xi] equation of state (EOS) with the parameters *a* and *b* proposed by Spycher *et al.*[xii] for CO_2

$$V^3 - \left(\frac{RT}{P_g}\right)V^2 - \left(\frac{RTb}{P_g} - \frac{a}{P_g\sqrt{T}} + b^2\right)V - \left(\frac{ab}{P_g\sqrt{T}}\right) = 0\,, \qquad (1)$$

where V is the molar volume of the CO_2, R is the gas constant, T is temperature, P_g is CO_2 pressure and a and b represent measures of intermolecular attraction and repulsion, respectively. If $a = b = 0$, then, the ideal gas law is recovered.

Given a CO_2 pressure P_g and a temperature T, Eq. (1) can be solved directly for V following a method like the one proposed by Nickalls[xiii].

Once the molar volume V is known, the CO_2 density, ρ_g, is calculated as

$$\rho_g = \frac{M_{CO2}}{V}\,, \qquad (2)$$

where $M_{CO2} = 0.044$ kg/mol is the CO_2 molecular weight (Figure 1a).

CO_2 viscosity is calculated using the expression proposed by Altunin and Sakhabetdinov[xiv]. This expression is a polynomial function of CO_2 density and temperature (Figure 1b). Additionally, water density increases as a result of CO_2 dissolution[xv], which allows reproducing density driven flow[xvi]. CO_2 enthalpy and CO_2 specific heat capacity are calculated also using the Redlich and Kwong[xi] EOS[xvii].

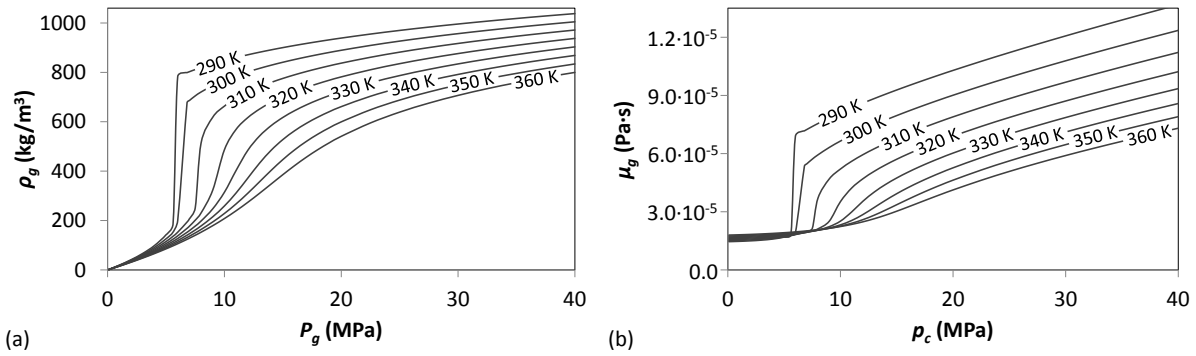

Figure 1. (a) CO_2 density and (b) viscosity as a function of pressure for several temperatures.

3. OVERPRESSURE EVOLUTION

The low viscosity of CO_2 and the two-phase flow nature of CO_2 flow in brine filled aquifers induce a practically constant overpressure after an initial sharp increase in pore pressure in the storage formation where CO_2 is injected (Figure 2). Such overpressure evolution has been measured in the field, e.g., at Ketzin, Germany[xviii]. This pressure evolution is very beneficial for maintaining the geomechanical stability of the rock, because the most critical situation occurs at the beginning of injection, which makes it easy to control. By contrast, the poromechanical response of the caprock induces an initial pore pressure drop[xix], which is known as reverse-water level fluctuation[xx]. Afterwards, fluid pressure increases because the overpressure of the aquifer induces a flow through the caprock. Actually, this flow of the resident brine across the caprock (and baserock) causes a decrease of the overpressure in the aquifer, decreasing the risk of inducing fault reactivation that could induce felt seismic events[xxi].

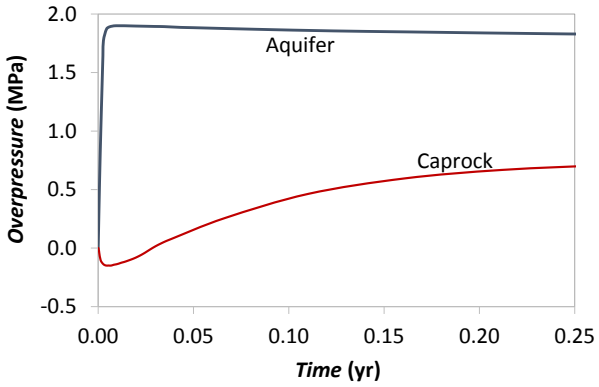

Figure 2. Overpressure evolution as a result of CO_2 injection in the aquifer and the caprock.

4. CAPROCK STABILITY

The low-permeability and high entry pressure of caprocks maintain CO_2 within the storage formation. However, an excessive overpressure may damage the caprock, which could eventually lead to CO_2 leakage[xxii]. Simulation results have shown that in order to reach shear failure conditions in the caprock, an overpressure higher than 50 % of the initial pore pressure and a very low strength of the caprock are necessary[xxiii]. If shear failure occurs in the caprock, the propagation pattern of inelastic deformation depends on the stress regime. Plastic strain propagates vertically in strike slip stress regimes, sub-vertically in normal faulting stress regimes and sub-horizontally in reverse faulting stress regimes[xxiv]. Thus, strike slip and

reverse faulting stress regimes may be less favorable than reverse faulting stress regimes because if failure of the caprock occurs, CO_2 may find a migration path through which it could reach freshwater aquifers or even the surface. Nevertheless, a proper pressure management should allow maintaining overpressure below the maximum sustainable injection pressure and thus, not compromising the caprock sealing capacity[xxv]. To determine the maximum sustainable injection pressure, a proper site characterization is required[xxvi,xxvii].

5. THERMAL EFFECTS

CO_2 will, in general, enter the storage formation at a colder temperature than that of the rock, forming a cold region around the injection well that propagates into the lower portion of the caprock (Figure 3). This cooling of the caprock has been feared to have the potential to form hydraulic fractures, through which CO_2 could penetrate into the caprock. Tensile failure may only occur in the presence of very stiff caprocks or for large temperature contrasts[xxviii]. Yet, failure conditions may not be reached into the caprock under these conditions because cooling of the aquifer causes stress redistribution that increases the horizontal stresses in the lower portion of the caprock, tightening it[vi]. The effect of this stress redistribution on rock stability depends on the stress regime, being especially beneficial for normal faulting stress regimes [xxix]. Thus, thermo-hydro-mechanical effects need to be investigated site specifically in order to determine both the maximum sustainable injection pressure and the maximum temperature drop that lead to a safe injection[xxx].

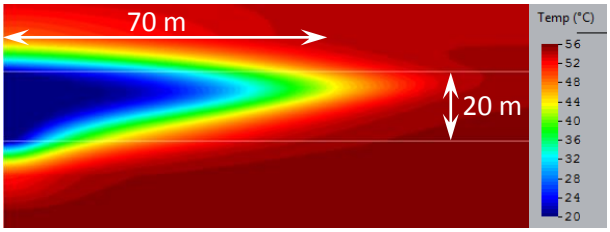

Figure 3. Temperature distribution after 2 years of injecting 0.2 Mt/yr of CO_2 at 20 °C. The two horizontal white lines indicate the limits of the 20-m thick storage formation.

6. CONCLUDING REMARKS

CODE_BRIGHT was extended to have CO_2 instead of air in the gas phase. This extension allows studying the complex coupled thermo-hydro-mechanical processes that occur in geologic carbon storage. The used EOS for describing the CO_2 properties are valid for a wide range of pressure and temperature conditions, including gas, liquid and supercritical states of CO_2. Our research has focused on understanding how CO_2 injection affects rock stability and on developing methodologies to determine safe injection conditions. A proper characterization of the thermo-hydro-mechanical properties of the aquifer and the caprock at the field scale is required to determine the maximum sustainable injection pressure and the maximum temperature drop that can be undergone safely. Additionally, a detailed pressure monitoring and analysis is necessary to detect heterogeneities that cause an unexpected increase in fluid pressure. If fluid pressure deviates from the expected one, pressure management should be performed to avoid causing fault reactivation that could induce felt seismicity. Overall, geologic carbon storage can be performed safely, i.e., with no CO_2 leakage and no felt earthquakes, provided that a proper site characterization and pressure management are performed.

REFERENCES

[i] IEA (2010). *Energy technology perspectives. Scenarios & strategies to 2050. Executive summary*, International Energy Agency.

[ii] Hitchon, B., Gunter, W.D., Gentzis, T. and Bailey, R.T. (1999). Sedimentary basins and greenhouse gases: a serendipitous association. *Energy Conversion & Management* 40:825–843.

[iii] Birkholzer, J.T., Zhou, Q. and Tsang, C.F. (2009). Large-scale impact of CO_2 storage in deep saline aquifers: a sensitivity study on pressure response in stratified systems. *International Journal of Greenhouse Gas Control* 3(2) :181-194.

[iv] Span, R. and Wagner, W. (1996). A new equation of state for carbon dioxide covering the fluid region from the triple-point temperature to 1100 K at pressures up to 800 MPa. *Journal of Physical and Chemical Reference Data* 25(6):1509-1596.

[v] Paterson, L., Lu, M., Connell, L.D. and Ennis-King, J. (2008). Numerical modeling of pressure and temperature profiles including phase transitions in carbon dioxide wells. *SPE Annual Technical Conference and Exhibition* Denver, 21-24 September 2008.

[vi] Vilarrasa, V., Silva, O., Carrera, J. and Olivella, S. (2013). Liquid CO_2 injection for geological storage in deep saline aquifers. *International Journal of Greenhouse Gas Control* 14:84–96.

[vii] de Simone, S., Vilarrasa, V., Carrera, J., Alcolea, A. and Meier, P. (2013). Thermal coupling may control mechanical stability of geothermal reservoirs during cold water injection. *Journal of Physics and Chemistry of the Earth* 64:117-126.

[viii] Vilarrasa, V., Rutqvist, J. and Rinaldi, A.P. (2015). Thermal and capillary effects on the caprock mechanical stability at In Salah, Algeria. *Greenhouse Gases: Science and Technology*, 5:1-13.

[ix] Olivella, S., Carrera, J., Gens, A. and Alonso, E.E. (1994). Non-isothermal multiphase flow of brine and gas through saline media. *Transport In Porous Media* 15:271–293.

[x] Olivella, S., Gens, A., Carrera, J. and Alonso E.E. (1996). Numerical formulation for a simulator (CODE_BRIGHT) for the coupled analysis of saline media. *Engineering Computations* 13:87–112.

[xi] Redlich, O. and Kwong, J.N.S. (1949). On the thermodynamics of solutions. V. An equation of state. Fugacities of gaseous solutions. *Chem. Rev*. 44:233-244.

[xii] Spycher, N., Pruess, K. and Ennis-king, J. (2003). CO_2-H_2O Mixtures in the Geological Sequestration of CO_2. I. Assessment and calculation of mutual solubilities from 12 to 100°C and up to 600 bar. *Geochim. Cosmochim. Acta* 67:3015-3031.

[xiii] Nickalls, R.W.D. (1993). A new approach to solving the cubic: Cardan's solution revealed. *Math. Gazette* 77:354-359.

[xiv] Altunin, V.V. and Sakhabetdinov, M.A. (1972). Viscosity of liquid and gaseous carbon dioxide at temperatures 220-1300 K and pressure up to 1200 bar. *Teploenergetika* 8:85-89.

[xv] Garcia, J.E. (2003). Fluid Dynamics of Carbon Dioxide Disposal into Saline Aquifers. PhD thesis, University of California, Berkeley.

[xvi] Saaltink, M.W., Vilarrasa, V., de Gaspari, F., Silva, O., Carrera, J. and Rötting, T.S. (2013). A method for incorporating equilibrium chemical reactions into multiphase flow models for CO_2 storage. *Advances in Water Resources* 62:431-441.

[xvii] Vilarrasa, V. (2012). Thermo-hydro-mechanical impacts of carbon dioxide (CO_2) injection in deep saline aquifers. PhD thesis, Technical University of Catalonia, Barcelona.

[xviii] Henninges, J., Liebscher, A., Bannach, A., Brandt, W., Hurter, S., Köhler, S. and CO2SINK Group (2011). *PT-ρ* and two-phase fluid conditions with inverted density profile in observation wells at the CO_2 storage site at Ketzin (Germany). *Energy Procedia*, 4:6085-6090.

[xix] Vilarrasa, V., Bolster, D., Olivella, S. and Carrera, J. (2010). Coupled hydromechanical modeling of CO_2 sequestration in deep saline aquifers. *International Journal of Greenhouse Gas Control* 4:910-919.

[xx] Hsieh, P.A. (1996). Deformation-induced changes in hydraulic head during ground-water withdrawal. *Ground Water* 34(6):1082-1089.

[xxi] Vilarrasa, V. and Carrera, J. (2015). Geologic carbon storage is unlikely to trigger large earthquakes and reactivate faults through which CO_2 could leak. *Proceedings of the National Academy of Sciences* 112(19):5938-5943.

[xxii] Rutqvist, J. (2012). The geomechanics of CO_2 storage in deep sedimentary formations. *International Journal of Geotechnical and Geological Engineering* 30:525–551.

[xxiii] Vilarrasa, V., Olivella, S. and Carrera, J. (2011). Geomechanical stability of the caprock during CO_2 sequestration in deep saline aquifers. *Energy Procedia* 4:5306-5313.

[xxiv] Vilarrasa, V., Carrera, J. and Olivella, S. (2013). Hydromechanical characterization of CO_2 injection sites. *International Journal of Greenhouse Gas Control* 19:665-677.

[xxv] Rutqvist, J., Birkholzer, J., Cappa, F. and Tsang, C.F. (2007). Estimating maximum sustainable injection pressure during geological sequestration of CO_2 using coupled fluid flow and geomechanical fault-slip analysis. *Energy Conversion and Management* 48(6):1798-1807.

[xxvi] Vilarrasa, V. and Carrera, J. (2015). Reply to Zoback and Gorelick: Geologic carbon storage remains a safe strategy to significantly reduce CO_2 emissions. *Proceedings of the National Academy of Sciences* 112(33): E4511-E4511.

[xxvii] Juanes, R., Hager, B.H. and Herzog, H.J. (2012). No geologic evidence that seismicity causes fault leakage that would render large-scale carbon capture and storage unsuccessful. *Proceedings of the National Academy of Sciences* 109(52):E3623-E3623.

[xxviii] Goodarzi, S., Settari, A. and Keith, D. (2012). Geomechanical modeling for CO_2 storage in Nisku aquifer in Wabamun Lake area in Canada. *International Journal of Greenhouse Gas Control* 10:113-122.

[xxix] Vilarrasa, V., Olivella, S., Carrera, J. and Rutqvist, J. (2014). Long term impacts of cold CO_2 injection on the caprock integrity. *International Journal of Greenhouse Gas Control* 24:1-13.

[xxx] Kim, S. and Hosseini, S.A. (2015). Hydro-thermo-mechanical analysis during injection of cold fluid into a geologic formation. *International Journal of Rock Mechanics and Mining Sciences* 77:220-236.

ON THE USE OF TIME STEP PREDICTION IN CODE_BRIGHT

Sebastia Olivella

Departament Enginyeria Civil i Ambiental, Escola de Camins, UPC BarcelonaTech

Introduction

CODE_BRIGHT uses dynamic time step variation under certain control conditions. In general, time step will tend to increase because time step is continuously increased by a factor of 1.4. User defined time step can be done according to the following set up:

Time begins at 0 days (**Initial Time**) and calculation will start with and initial time step of 0.001 (**Initial Time Step**). Calculation should continue until 100 days (**Final Time**). Time step will increase until 0.5 (**Partial Time**) from the initial value of 0.001. After 0.5 days, time step can increase until it reaches the value of 1.0 (**Partial Time Step**), which is the maximum time step permitted. **Partial Time** can be equal to **Initial Time** or **Final Time**. Interval 1, going from 0 to 100 days is shown in the window. **Initial Time** for a second interval should be set equal to **Final Time** of the first interval. Several Intervals can be considered.	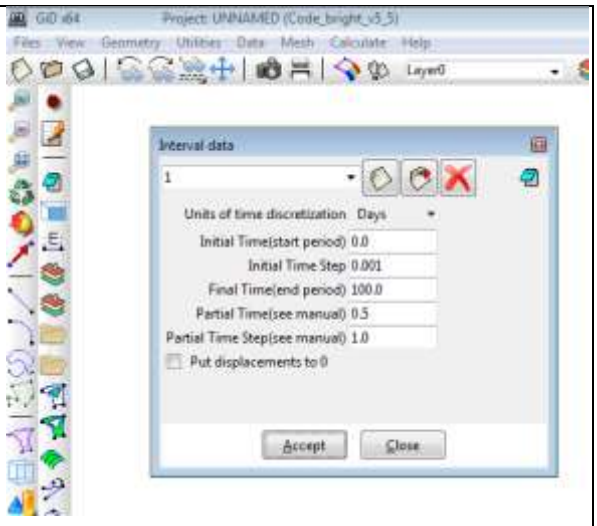

Time step control can be done by trial and error procedure. This means that a time step is proposed and calculations proceed. Rejection of time step and restart calculations with a new one is done whenever one of the following problems during Newton Raphson iteration, appears:

- Number of iterations: When the maximum number of iterations (user defined value) is reached without convergence being achieved, current time step is rejected. A new time step is calculated by reducing the current one and new calculations are carried out. In this case time step is reduced by a factor of 2 as there is no additional information to use other values.
- Increasing corrections (divergence of NR algorithm): When a variable shows systematic values of corrections that increase during Newton Raphson iterations, the current time step is rejected and a smaller one is considered. Again a reduction by a factor of 2 is considered.
- Large corrections: When a variable undergoes a large correction during Newton Raphson calculations, the calculations for a given time step are stopped. Time step is reduced using a scaled value which is obtained from the large variation obtained and the user defined maximum variation permitted. For instance if temperature variation is permitted up to 1^{o} C and corrections indicate a variation of 3^{o} C, time step would be reduced by a factor or 3. A lower bound is considered.

Time step prediction

A number of options are available in CODE_BRIGHT (Olivella et al 1996) to perform a time step prediction. The objective of time step prediction is to reduce the numerical error of the calculated results. A consequence of good time step prediction must be the reduction of time step rejections. A strict time step prediction may produce a large CPU-time needed to finish the calculation as time step becomes very small. It is desirable to obtain results with low error using an acceptable numerical effort.

A time step prediction scheme has to be chosen for every specific problem. It may depend on accuracy required or desired, non-linearity of the constitutive equations (and this depends on parameters), quality of the mesh, and boundary conditions (instantaneous changes, presence of ramps, non-linear boundary conditions i.e. the ones that depend on the variable at node).

A strict time step prediction scheme may produce good results for a relative simple problem (depending on non-linearity and quality of the mesh) and fail for more complex problems. Failure of time step prediction happens when the estimated errors cannot be limited by time step reduction. In such case, time step prediction gives rise to very small time steps and the calculation fails to advance until end of the calculation.

The following is a list of options for time step prediction (in CODE_BRIGHT) based on different criteria.

Time step prediction	**Description of time step prediction**
0	No time step prediction. Maximum number of NR iterations = 10 (*). Maximum variations for time step rejection = 0.1 m, 10 MPa, 0.1 C. This is maintained in all cases.
Method based on the number of NR number of iterations	
1, 2, 3	Time step prediction according to an expected target of 4, 3, or 2 iterations per time step.
Method based on error estimation of unknowns	
6	A new time step is predicted from the relative error in variables of the previous time step calculation (see below for more detailed description). If the relative error is greater than *dtol* = 0.01, time increment is reduced according to error deviation, otherwise it is increased. (Kavetsky et al, 2002).
7, 8, 9, 10	The same as 6, but with *dtol* = 0.001, 0.0001, 0.00001, 0.000001, respectively
Method based on error estimation combined with second order equation	
16 to 19	The same as 6 to 9 but second order equation (see below)
Method based on error on stress update	
42	A new time step is predicted from the error in stresses of the previous time step calculation. If the relative error is greater than *dtol* = 0.1, time increment is reduced according to error deviation.
43, 44, 45	The same as 41, but with *dtol* = 0.01, 0.001, 0.0001, respectively.

Description of time step prediction options

Option 0

No time step prediction is performed. Time step is controlled by the user given values according to the time interval definition window (see above). An upper bound of time step is considered. Time step rejections (and subsequent reductions) can occur if convergence is not achieved or other reasons.

Convergence implies that time step will be increased by a factor of 1.4 regardless of the number of iterations or evolution of errors. IF the user defined value of maximum number of iterations is reached, time step is reduced by a factor of 0.5. On the other hand, if large variations of displacements, pressures or temperatures occur during a NR iteration, time step is reduced immediately simply by scaling, and calculations start again for the current time step.

The values considered in the calculations in this paper are: Maximum number of NR iterations = 10. Maximum variation for time step rejection, of displacement, pressure and temperature = 0.1 m, 10 MPa, 0.1 C, respectively. For instance, if temperature variation is 0.5, time step is reduced by 1/5. Time step rejections are not desirable, but can occur. This is maintained in all cases. Rejections are large for Option 0 (no time step prediction is performed), but decrease as a time step prediction method is considered.

Options 1, 2, 3

The number of Newton Raphson iterations is used to estimate the value of the time step that will be used after convergence for the next time step calculation. There are three possibilities in this case according to 4, 3 or 2 Newton Raphson iterations.

Time step control value (ITIME) = 1, 2, 3

$$f = \left(\frac{4}{iter}\right)^{0.25} \geq 0.5,\ f = \left(\frac{3}{iter}\right)^{0.25} \geq 0.5,\ f = \left(\frac{2}{iter}\right)^{0.25} \geq 0.5$$

The value of *f* has an upper bound of 1.4. Note that *f* = 1 when the target of number of iterations is obtained and this implies same time step.

Options 6, 7, 8, 9, 10

An estimation of error (for displacements, pressures and temperatures) is used to predict time step (kavetsky et al 2002). Time step is predicted with the factor *f* which is calculated with:

$f = 0.8\left(\frac{DTOL}{error}\right)^{0.5}$ with $0.1 \leq f \leq 1.4$	The value of *DTOL* has the following values depending on the option chosen: *6* - *DTOL* = 0.01 (not used in this study), *7* - *DTOL* = 0.001, 8 - *DTOL* = 0.0001, 9 - *DTOL* = 0.00001, 10 - *DTOL* = 0.000001 (used in this study to obtain a reference solution).

The variable *error* is calculated using an error estimator based on second order prediction. An upper and lower bound for *f* are considered.

Options 16, 17, 18, 19

Same as 6,7,8,9 but second order approximation of conservation equations is used. This is based on the following equations (for implicit scheme):

$$\left(\frac{2\left(\mathbf{m}(\mathbf{x}_n) - \mathbf{m}(\mathbf{x}_{n-1})\right) - h\dot{\mathbf{m}}(\mathbf{x}_{n-1})}{h}\right) + \left[\mathbf{K}(\mathbf{x}_n)\right]\mathbf{x}_n = \mathbf{F}_n$$

This is a modification of the usual approach in CODE_BRIGHT which can be written in the following compact way:

$$\left(\frac{\mathbf{m}(\hat{\mathbf{x}}_n) - \mathbf{m}(\mathbf{x}_{n-1})}{h}\right) + \left[\mathbf{K}(\hat{\mathbf{x}}_n)\right]\hat{\mathbf{x}}_n = \mathbf{F}_n$$

If the maximum time step prescribed manually (DTIMEC) is achieved, time step will not increase furthermore.

Options 42, 43, 44, 45

An estimation of error (stresses) is used to predict time step. Time step is predicted with the factor *f* which is calculated with:

$f = 0.8\left(\frac{DTOL}{error}\right)^{0.5}$ with $0.1 \leq f \leq 1.4$	The value of *DTOL* has the following values depending on the option chosen: 42 – *DTOL* = 0.01, 43 - *DTOL* = 0.001, 44 - *DTOL* = 0.0001, 45 - *DTOL* = 0.00001

The variable *error* is calculated using an error estimator for stresses. The variable *f* is the factor for time step reduction. An upper and lower bound for *f* are considered.

Results obtained and conclusions

A simulation of a typical Mock-Up experiment (a simulated waste surrounded by unsaturated clay) is used to do several run tests to determine various aspects such as the error of results, the CPU time and the number of iterations (see general description of Modelling Mock-up test in Gens et al 1998).

The geometry of the model is very simple. Boundary conditions are simple as well. Normal displacements are prescribed on all boundaries. Heating takes place on the inner boundary (representing the heating effect of a canister) and water pressure is prescribed on the outer boundary (representing the hydration effect from the rock).

Time days	*Time seconds*	*Boundary condition changes*
0 to 6	0 to 5.184×10^5	Constant temperature (20oC) and pressure (0.55 MPa) on the outer boundary. Maintained until end. 130 W/m2 on the internal boundary.
6 to 20	to 1.728×10^6	Power increased to 260 W/m2 on the internal boundary.
20 to 30	to 2.592×10^6	Power decreased to 250 W/m2 on the internal boundary.
30 to 60	to 5.184×10^6	No changes
60 to 2000	to 1.728×10^8	No changes
2000 to 3000	to 2.592×10^8	Power shut down to 0 W/m2 on the internal boundary.

Intervals without changes in boundary conditions are included in this table as these may produce changes on the time step.

Evolution of temperature, liquid pressure and mean stress is represented for 3 points in the domain in Figure 1. Temperature evolution shows the effect of the heat inflow into the model. Due to heating, water evaporates and liquid pressure reaches -200 MPa near the hottest surface. Due to progressive hydration, mean stress increases. Temperature decreases rapidly when the heat inflow is stopped. Due to cooling, hydration accelerates and the porous medium becomes fully saturated. Due to cooling, stress decreases somewhat but continues increasing due to water inflow.

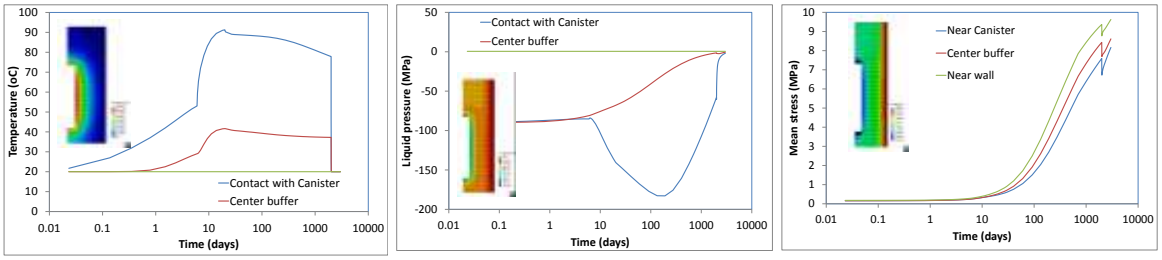

Figure 1. Temperature, liquid pressure and mean stress for a simple Mock-up model simulation.

A reference case that uses very small time steps is used to determine the error of each run by comparison. This very small time step case uses one Newton Raphson iteration for every time step during the calculation as the time step is so small that corrections at every time step are smaller than tolerances. This is achieved with *DTOL* = 0.000001 (Option 10).

Error for each method is calculated as the difference between the calculated results at the at 60 days. This can be done for unknowns (displacement, pressure, temperature) or for any other variable. The maximum variable relative error for all nodes is compared. Figure 2 shows errors for each option.

In general, the errors decrease when the time step prediction scheme becomes stricter. For instance, when the tolerance *DTOL* is decreased, the errors decrease (options 7-8-9). The errors decrease near one order of magnitude when option 8 is used instead of 7, or when option 9 is used instead of 8. Options 7, 8 and 9, show consistent error reduction.

Options 1, 2 and 3 also show reduction of errors, but less consistently. This is expected as this method is not based on error, but on the number of NR iterations.

Options 2 and 7, show similar errors, so although correspond to different strategies they can be considered equivalent.

Options 17, 18 and 19 do not improve the errors obtained by 7, 8 and 9 (or 1, 2 and 3). Options 43, 44, 45 do not improve the errors obtained by the other methods.

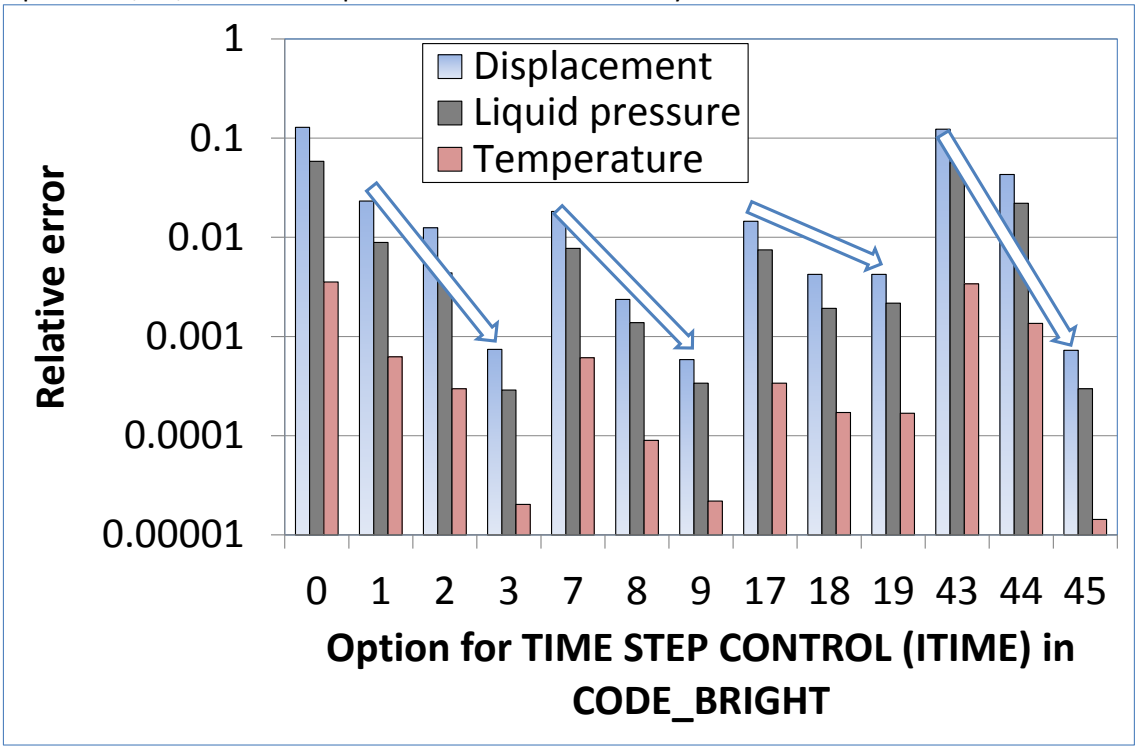

Figure 2. Relative error for displacements, liquid pressures and temperatures calculated at 60 days for each option. Temperatures show less error than liquid pressures which in turn give fewer errors than displacements. 7, 8 and 9 show error decreases that are consistent with the tolerance considered. The set of options 17, 18 and 19 do not improve the errors. Neither the set of options 17, 18, 19. Options 1, 2, 3 show a similar response as 7, 8, 9.

In order to make, decisions it is important to know the cost for each method. CPU time is normalized with respect to the CPU time required to solve case "0" (Figure 3).

The maximum value recorded by the different time step prediction options is 9 times (option 45). CPU time becomes larger mainly because time step is smaller. Smaller time steps imply lower number of NR iterations. The fact that lower NR iterations are used does not compensate the effect of more time steps. Hence, smaller time steps always imply more CPU time.

The number of NR iterations ranges between 1 and 3 in average. When the average is 1, it means that all time steps require only one Newton - Raphson iteration. This happens when time step is very small as it cannot grow due to error control. One Newton - Raphson iteration means that the projection (from previous time step calculations, variables are projected linearly) becomes very close to the solution.

Option 2 leads to 2.5 NR iterations per time step. CPU time is moderately bigger than the reference case Option 0. Error in variables is approximately 10 times lower than the reference case Option 0. Hence, this is a recommended option.

Option 8 leads to 2 NR iterations per time step. CPU time is 3 times the reference case. Error in variables is about 20-30 times lower than the reference case Option 0. This is an interesting option provided that an increase of CPU time is accepted.

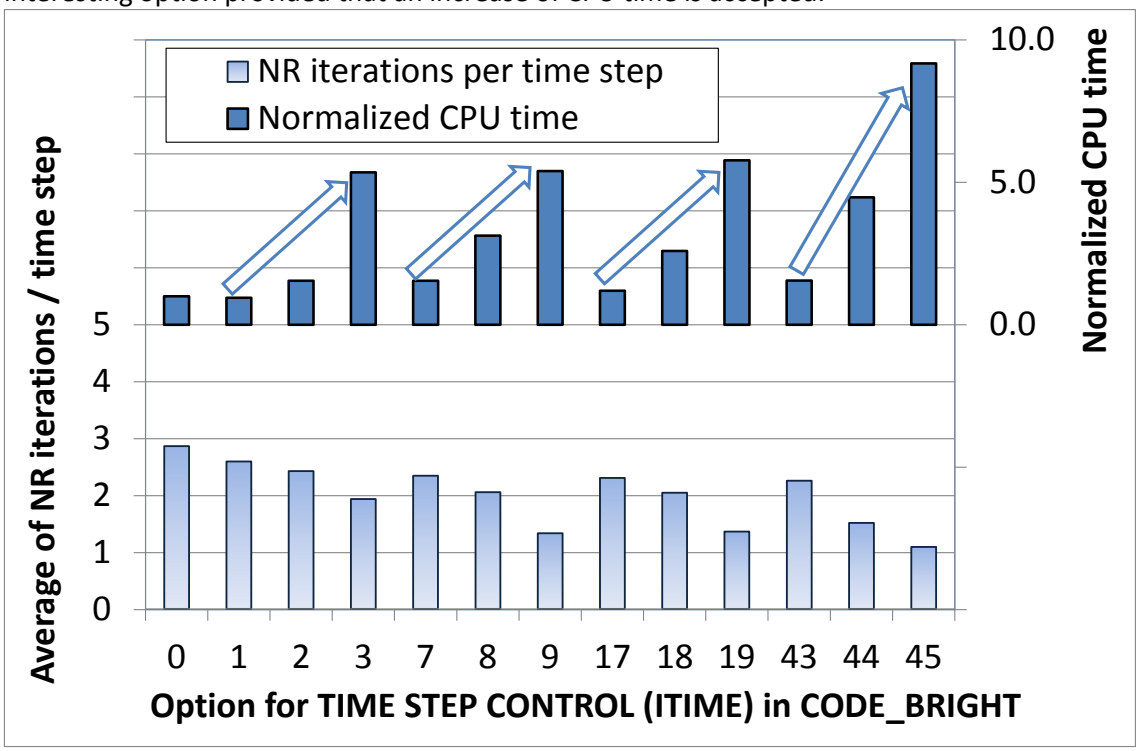

Figure 3. Normalized CPU time and average number of NR iterations for model runs with different options for time step predictions. CPU time increases when "time step control" method is stricter because time steps are smaller. This is compensated by the reduction on the number on NR iterations.

References

Gens, A., A.J. Garcia-Molina, S. Olivella, E. E. Alonso, F. Huertas. (1998) Analysis of Full Scale In-situ Heating Test Simulating Repository Conditions. International Journal for Numerical and Analytical Methods in Geomechanics. 22:515-548.

Kavetski, D. Binning, P. and Sloan S.W., Adaptive backward Euler time stepping with truncation error control for numerical modelling of unsaturated fluid flow, Int. J. Numer. Meth. Engng 2002; 53:1301–1322 (DOI: 10.1002/nme.329)

Olivella, S., A. Gens, J. Carrera, E. E. Alonso, (1996), Numerical Formulation for a Simulator (CODE_BRIGHT) for the Coupled Analysis of Saline Media, Engineering Computations, Vol. 13, No 7, , pp: 87-112.